INTERNATIONAL JOURNAL OF CIRCUIT THEORY AND APPLICATIONS
Int. J. Circ. Theor. Appl. 2018; **46**:155–183
Published online 4 December 2017 in Wiley Online Library (wileyonlinelibrary.com). DOI: 10.1002/cta.2431

SPECIAL ISSUE PAPER

Memristor-enhanced humanoid robot control system – Part I: Theory behind the novel memcomputing paradigm

A. Ascoli[1,*,†], D. Baumann[2], R. Tetzlaff[1], L. O. Chua[3] and M. Hild[4]

[1]*Institute of Circuits and Systems, Faculty of Electrical and Computer Engineering, Technische Universität Dresden, Dresden, Germany*
[2]*Autonomous Motion Department, Max Planck Institute for Intelligent Systems, Tübingen[‡], Germany*
[3]*Department of Electrical Engineering and Computer Sciences, University of California Berkeley, Berkeley, California, USA*
[4]*Fachbereich VII, Forschungslabor Neurorobotik, Beuth Hochschule für Technik Berlin, Berlin, Germany*

SUMMARY

Myon is a humanoid robot where each joint is controlled independently by a supervised bio-inspired artificial neural network inducing the correction of a number of distinct actions depending on the excitation. One of the control strategies, which the network, located within a certain joint, may implement, allows a controlled motion of the limb connected to the joint from a stable state up to a prescribed height and the maintenance of the new position afterwards. The original approach adopted for this control operation is stable and robust but results in slow and energy-inefficient limb movements. This work proposes a novel, low-power, time-efficient and adaptive memristor-centred control strategy for the aforementioned robot action. The idea is based upon the exploitation of the combined ability of memristors to store and process data in the same physical location. The part I paper sets the theoretic foundations for the memcomputing paradigm to robot motion control, while the part II manuscript shall demonstrate its benefits over the original approach in terms of energy, and speed, and the inheritance from the standard strategy of a good level of adaptability to changes in the limb load on the basis of the analysis of circuit-theoretic models adopting an ideal and a real memristor, respectively.

Received 3 August 2017; Revised 26 September 2017; Accepted 3 October 2017

KEY WORDS: memristor; circuit theory; nonlinear dynamics theory; control theory; adaptive circuits; robotics

1. INTRODUCTION

Before 1971, only three fundamental passive one ports were known in circuit theory [1], namely, the resistor, in which voltage v and current i are constrained to obey a law of the form $f_R(v, i) = 0$, the capacitor, characterised by a constitutive relationship involving voltage v and charge q, namely, $f_C(q, v) = 0$, and the inductor, whose dynamic operation is governed by a rule involving current i and flux φ, that is, $f_L(\varphi, i) = 0$. In 1971, through symmetry arguments, Chua [2] theoretically predicted the existence of a fourth fundamental passive two-terminal device, which he named memory resistor (memristor for short), establishing a nonlinear relation between charge q, the time integral of current (called current momentum in [3]), and flux φ, the time integral of voltage (called voltage momentum in [3]), in the form $f_M(\varphi, q) = 0$. For more than 35 years, research in the area of memristors involved only theoretical aspects. In 2008, a team from Hewlett Packard Labs, led by senior fellow R. S. Williams, announced the development of a two-terminal nanoscale device featuring some of the fingerprints of memristor

*Correspondence to: Alon Ascoli, Institute of Circuits and Systems, Faculty of Electrical and Computer Engineering, Technische Universität Dresden, Dresden, Germany.
[†]E-mail: alon.ascoli@tu-dresden.de

behaviour [4]. Since then, besides some major advancement in memristor theory [5–10], the potential benefits associated with the adoption of memristors [11, 12] in future electronics have been extensively investigated in various areas of circuit design, including oscillators [13–16], neuronal networks [17–21], tunable amplifiers [22], adaptive filters [23, 24] and control circuits [25, 26]. Leveraging the peculiar nonlinear dynamics of memristors [27], originating from distinct physical mechanisms, depending upon constitutive material, fabrication process and operating regime, novel approaches to data sensing [28] and processing [29, 30] may be developed and implemented in circuit form. Furthermore, the unique capability of nonvolatile memristors to store and process data in the same physical location can pave the way towards the design of innovative memcomputing (i.e. memory and computing) hardware systems [31] resolving the throughput limitation of classic von Neumann architectures.

The realisation of humanoid robots is described [32] as the challenge *par excellence* for researchers in the field of artificial intelligence and robotics. Currently, a great deal of studies are devoted to the development of robots capable to perform a number of different tasks [33] depending upon external stimuli. Among the various functionalities, a humanoid robot should be endowed with the ability to lift a limb from a rest position up to a specific height, and to keep it there till the completion of a certain operation [34] (the focus of this research work), as well as the capability to exhibit a stable and fast walking pattern [35, 36] are definitely worth a mention.

Typically, the control of a humanoid robot is based upon the selection of a certain strategy, the development of a model for its implementation, the coding of the mathematical description through a proper programming language and the final code execution through the use of suitable microcontrollers. In the humanoid robot Myon [37] (Figure 1(a)) a completely different control approach is employed. Each of its joints hosts a cognitive densorimotor loop (CSL), trained – through an attractor-based behaviour control learning scheme [38] – to implement various control strategies depending upon how it is stimulated. The supervised loop is an innovative bio-inspired artificial neural network (ANN) exploiting only the inherently complex behaviour of an ensemble of analogue electrical circuits, based upon the standard complementary metal oxide semiconductor (CMOS) technology, to control the associated joint independently from the rest of the robot body through the crucial interaction with a motor with

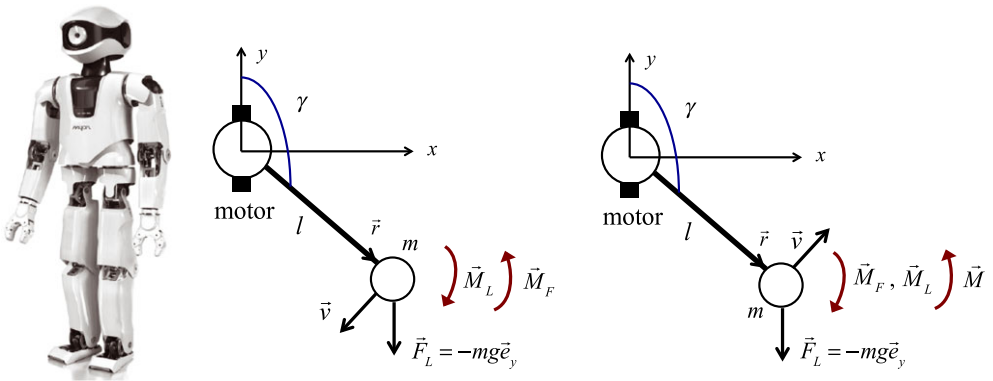

Figure 1. (a) The humanoid robot Myon. (b and c) An inverted pendulum, the simplest model of one of Myon's joint-limb structures, during a typical sense phase (b) and drive phase (c) under the hypothesis $\gamma \in [0, \pi]$ ($\vec{r} = l \sin\gamma\, \vec{e}_x + l \cos\gamma\, \vec{e}_y$ is the position vector). Apart from an initial short time interval, in which, driven by the momentum gained in the previous drive phase, the load ascent may persist, the pendulum typically moves downwards in a sense phase (b); thus, the sensed signal v denotes a rate of descent, which is negative (positive) for clockwise (counterclockwise) rotation under $\gamma \in [0, \pi]$ ($\gamma \in [-\pi, 0]$). Because the sensed signal is integrated with negative sign in the sense phase, a net positive (negative) direct current voltage is available at the integrator output at the end of the sensing operation under $\gamma \in [0, \pi]$ ($\gamma \in [-\pi, 0]$). This direct current voltage is applied to the motor input stage in the drive phase, and, thanks to the sign reversal introduced by the cognitive sensorimotor loop feedback loop, results in the generation of a torque $\vec{M}$ counteracting the effects of the gravitation torque $\vec{M}_L$ (c). Induced by the acceleration gained in the preceding sense phase, the pendulum descent may go on initially for a little while, but the pendulum typically moves upwards in a drive phase (c); thus, $\vec{M}$ also goes against the friction torque $\vec{M}_F$. [Colour figure can be viewed at wileyonlinelibrary.com]

DOI: 10.1002/cta

combined sensor–actuator role [34]. One of the CSL strategies, the so-called 'Go-Against-the-Force' (GAF) paradigm, leverages the nonlinear dynamics of an electromechanical system to induce a limb to move from a rest location up to a desired height, which is further stabilised thereafter. As mentioned earlier, a key role in the electromechanical system is played by a motor, which alternately plays the role of a sensor and of an actuator, during consecutive sense and drive phases, respectively. In sensing mode, the pendulum typically falls down because of gravitation, while a physical quantity proportional to its angular velocity is sensed via the motor electromotive force and integrated with negative sign. In driving mode, the direct current (DC) voltage at the output of the inverting integrator at the end of the previous sense phase is applied to the armature node of the rotor stage, resulting in the generation of a motor torque, which counteracts and wins over the gravitation torque, lifting the pendulum up.

Despite being stable and robust [39], the GAF control paradigm has its own weaknesses when it comes to energy efficiency and speed. Here, we demonstrate that these issues may be resolved through the introduction of a novel control strategy, which we name 'Kick-Fly-Catch' (KFC) paradigm and consists of three main phases. In the first kick phase, the system is driven with the maximum possible DC voltage available to the overall circuit, leading to a fast ascent of the pendulum towards the target upright position. In the second fly phase, no control is applied to the pendulum, while its angular velocity, or, equivalently, its axial velocity, is continuously monitored to detect any polarity change (here, the pendulum has come to a halt and is starting its descent from the same side from which it ascended) or magnitude increase (here, the pendulum has passed over the upright position and is starting to move down from the other side with respect to the one from which it ascended). Should one of these two events be detected, the third catch phase, which consists of an iterative cycle of sensing and driving operations, as established by the GAF strategy protocol, would commence, allowing to stabilise the pendulum in the upright position. Because here the lengthy and energy-consuming GAF control paradigm is applied only when the pendulum is about the unstable target state, the proposed procedure outperforms the standard approach in terms of limb motion speed and energetic cost. A crucial operation in the proposed paradigm is the derivation of an appropriate estimate for the time duration of the current kick phase. In order to fulfil this task, we apply a procedure revolving around the memcomputing capability of a nonvolatile memristor [2, 27]. Throughout the previous catch phase, the device is directly stimulated with the first inverting integrator output voltage. The resulting change in memristance, proportional to the stimulus time integral, updates the device resistance value, which represents the current estimate for the 'work' necessary to lift the pendulum from the stable rest state to the unstable upright position.[‡] During the current kick phase, the time integral of the DC armature voltage is a linear function of time. When this function equals the aforementioned pendulum lift 'work' estimate, the fly phase sets in.

So, over a catch phase, the memristor computes the non-inverting integration of the stimulus applied across it through the time evolution of its resistance. However, the memristor is also used to store the result of this integration from the end of the current catch phase to the beginning of the next catch phase, when it is retrieved to update the pendulum lift 'work' estimate, and, consequently, the time duration of the next kick phase, demonstrating, especially under perturbations to the system initial conditions or under modifications in the pendulum geometry, a good degree of adaptability to the external environment, similarly as in the standard GAF control approach. The non-inverting integration of the inverting integrator output voltage over a catch phase could also be carried out by a capacitor, which, however, would not exhibit the same capability of a nonvolatile memristor to keep the information embedded in its state for a very long time, as could be necessary in case a lengthy time interval would separate the end of a catch phase from the beginning of the next one. This would happen, for example, in case the robot is turned off for some time between two consecutive KFC strategy runs.

All in all, in this paper, we provide the theoretic foundations of the innovative memristor-centred KFC control approach, which allows the robot to exhibit faster movements under lower energy bud-

[‡]Before the first application of the KFC strategy, the old GAF paradigm is preliminarily run with the pendulum initially around the stable rest state to derive an initial estimate for the 'work' necessary to lift it up to the unstable upright location. By applying the inverting integrator output voltage across the nonvolatile memristor throughout the GAF strategy application, the change in device memristance, proportional to the stimulus time integral, provides an initial estimate for the aforementioned pendulum lift 'work'.

DOI: 10.1002/cta

get requirements as compared with the original method, without any compromise on stability and robustness. The memcomputing capability of a nonvolatile memristor is the key feature allowing the determination of the optimal time instant at which the kick phase should give way to the fly phase, and its update over successive applications of the KFC strategy, a clear example of unsupervised learning, resulting in a control system capable to adapt to perturbations to the initial conditions or to changes in the limb topology. In the companion part II paper [40], different memristor models – including an ideal device [41] and a real component [42] from Knowm, Inc. [43] – have been considered in the mathematical description and circuit implementation of the proposed control approach. This work provides a clear example of the novel functionalities the peculiar nonlinear dynamics of memristors [44] may endow electronic circuits with, justifying the enormous research efforts currently devoted to the theory and applications of these devices.

2. GO-AGAINST-THE-FORCE STRATEGY OF THE COGNITIVE SENSORIMOTOR LOOP

As mentioned in Section 1, the CSL is a supervised ANN implemented in circuit form in each joint of Myon through an ensemble of CMOS-based analogue electronic systems, coupled to a motor, which, over the course of the control action, acts consecutively as a sensor or as an actuator to provide signals to be processed by the loop circuitry or to be applied to a given target to correct its operation, respectively. One of the most important control strategies, which the CSL circuitry may implement independently in each joint, is the movement of the limb connected to it from a rest position up to a certain height and the maintenance of this new state thereafter. In this section, we shall describe the classical GAF approach adopted for this control system in the current implementation of Myon. In Section 2.1, a closed-loop circuit implementation of the original control strategy shall be presented. In Section 2.2, on the basis of LTSpice simulations [45] of the circuit implementation, we shall discuss the performance issues of the GAF paradigm. In Section 3, we shall explain how these issues may be overcome by introducing a novel control strategy revolving around the peculiar nonlinear dynamics of a nonvolatile memristor. In the companion part II paper [40], adopting a couple of distinct memristor models, one from the class of ideal memristors and the other describing the dynamics of a real nanodevice from Knowm, Inc. [43], circuit theoretic models for the implementation of the KFC control paradigm shall be first developed and then simulated in the LTSpice simulation environment to validate the theoretical findings provided in this part I paper.

The GAF control strategy is based upon the consecutive alternation of two phases, consisting of sensing and driving operations. In order to simplify the analysis, in this manuscript, we shall often refer to the simplest model of a humanoid robot's joint-limb structure, consisting of an inverted pendulum with a rod of length l, forming an angle[§] γ with the unit vector $\vec{e}_y$ and having upper and lower ends coupled to a motor and to a load of mass m, respectively. Throughout this study, we typically choose the stable rest state, where $\gamma = \pi$, or a position nearby as initial pendulum location, and the unstable upright point, where $\gamma = 0$, as final desired pendulum destination, but straightforward modifications to the control scheme may permit the limb to be repositioned elsewhere. Figure 1(b) refers to a typical scenario during the sense phase, where the pendulum is left free to move autonomously and the motor acts merely as a sensor, capturing a signal proportional to the load axial velocity[¶] v, which is simultaneously processed by the GAF control loop, taking its time integration while changing its sign, a clear example of negative feedback action. Figure 1(c) shows a common situation during the drive phase, where the pendulum is driven by the motor, taking the role of an actuator as it exerts a torque $\vec{M}$ to the load[‖] to counteract the effects of the external torque $\vec{M}_L$ due to gravitation and lift the pendulum up.

The block diagram of the classical GAF control technique applied in the current implementation of Myon to perform the aforementioned limb repositioning is shown in Figure 2(a). The alternating

[§] Angle values are measured in rad throughout this paper as well as in the companion part II manuscript [40].

[¶] More precisely, the sensed signal is proportional to the load angular velocity ω, which, however, is proportional to and has the same sign as the load axial velocity v, as shown later.

[‖] At the end of the sense phase, the result of the aforementioned inverting integration is a DC voltage, which, applied to the motor input stage, allows the generation of the 'GAF' torque $\vec{M}$.

DOI: 10.1002/cta

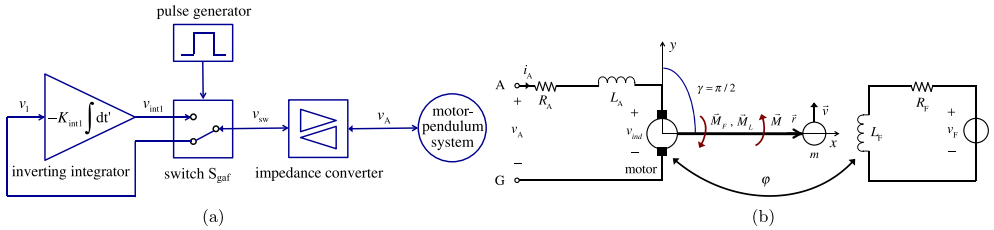

Figure 2. (a) Block diagram of the classical Go-Against-the-Force strategy a cognitive sensorimotor loop implements independently in each joint to raise a limb from a rest position up to its maximum height and to stabilise it there afterwards. The lower (upper) switch position allows the implementation of the sense (drive) phase of the paradigm. The motor-pendulum system represents the stator, the rotor (composed of the motor and its input stage) and the loaded rod attached to the motor. (b) Electromechanical model of the motor-pendulum system. In the sense phase, the voltage at node A is transferred to the input of the inverting integrator (thus $v_1 = v_A$ in plot (a)), consequently $i_A = 0$ A, and, typically, a sign-inverting integration of the load rate of descent, which is negative (positive) under $\gamma \in [0, \pi]$ ($\gamma \in [-\pi, 0]$), is available at node at voltage v_{int1} in plot (a). In the drive phase, the result of the integration, a net positive (negative) voltage under $\gamma \in [0, \pi]$ ($\gamma \in [-\pi, 0]$), is applied as direct current stimulus to node A, enabling the generation of a torque $\vec{M}$ lifting the loaded pendulum up. The torques shown here refer to a particular case of a drive phase, when the position vector is expressed by $\vec{r} = l\,\vec{e}_x$, because the loaded rod coupled to the motor forms an angle γ of $\pi/2 = 1.57$ with the unit vector $\vec{e}_y$ (here, $|M_L|$ attains its maximum possible value). [Colour figure can be viewed at wileyonlinelibrary.com]

repetition of sensing and driving operations is enabled by a pulse-controlled switch, referred to as S_{gaf}, which configures the motor as sensor or actuator in a sense and drive phase, respectively. Let us explain the operation of each block in Figure 2(a). The block named motor-pendulum system, including the stator, the rotor (consisting of the motor and its input stage) and the loaded rod attached to the motor, has the detailed electromechanical representation shown in Figure 2(b) [46]. The left-placed stage is the rotor. The motor input stage, also known as armature circuit, is a two port, consisting of the series between the armature resistance R_A and the winding leakage inductance L_A, which couples the motor to the impedance converter of Figure 2(a), used to reduce by a factor 10^3 the current flowing into its left terminal with respect to the current flowing into its right terminal while constraining the voltages v_{sw} and v_A to follow each other. The input port voltage of the armature circuit, denoted as v_A, is referred to as armature voltage, because it coincides with the voltage at the armature node A, given that node G is connected to ground. The armature node plays a fundamental role in the control strategy. In fact, referring to Figure 2(a), it is the voltage at this node, which is sampled and processed in the sense phase, when the switch S_{gaf} is configured in the lower position. Thus, in this phase, the armature circuit input port current i_A, known as armature current, is null, the voltage v_A under sensing coincides with the output port voltage of the armature circuit, denoted as v_{ind}, and standing for the electromotive force falling across the motor terminals, and the load is only subject to gravitation and friction torques $\vec{M}_L$ and $\vec{M}_F$, respectively (Figure 1(b)). The motor voltage v_{ind} is proportional to the load axial velocity v. So, effectively, during a sense phase, the control loop of Figure 2(a) typically performs a sign-inverting integration of the load rate of descent, which is negative (positive) under $\gamma \in [0, \pi]$ ($\gamma \in [-\pi, 0]$). The result of the CSL feedback loop computation at the end of the sense phase, a net positive (negative) voltage under $\gamma \in [0, \pi]$ ($\gamma \in [-\pi, 0]$), is then applied as a DC voltage to the armature node in the drive phase, when the switch S_{gaf} in Figure 2(a) is clicked into the upper position, resulting in the flow of a positive (negative) armature current i_A into the motor input stage of Figure 2(b) and leading to the generation of a torque $\vec{M}$ pointing in the same (opposite) direction as (to) the unit vector $\vec{e}_z$ and thus acting on the load to compensate the gravitation torque and induce its ascent (see the typical scenario in Figure 1(c)). This clarifies the origin for the name adopted for the standard control paradigm, namely, 'Go-Against-the-Force', which highlights the negative feedback action resulting from the use of an inverting integrator in the CSL circuitry.

The right-placed stator stage in the electromechanical model of the motor-pendulum system of Figure 2(b), also known as field circuit, is a one port generating a magnetic flux φ, which, as reviewed shortly, has a direct impact on the electromotive force v_{ind} as well as on the torque $\vec{M}$, which the

DOI: 10.1002/cta

motor exerts on the load in the drive phase. The field circuit is composed of the series between the coil inductance L_{F}, its parasitic resistance R_{F} and a voltage source v_F. The magnetic flux has expression $\varphi = L_{\mathrm{F}} i_{\mathrm{F}}$, where i_{F} may be determined by solving the Kirchhoff voltage law (KVL)-based equation $v_{\mathrm{F}} = R_{\mathrm{F}} i_{\mathrm{F}} + L_{\mathrm{F}} \frac{di_{\mathrm{F}}}{dt}$ under a certain stimulus v_{F}. Assigning a positive DC value to the latter, as is the case in the system under focus here, φ is constant and positive at all times. A rod, attached to the motor on one side and to a load on the other side, is also visuald in Figure 2(b) as it ascends during a drive phase.

Let us now go through the mathematical analysis of the system under control. With reference to Figure 1(b) and (c), the angular velocity $\vec{\omega}$ of the pendulum is defined as

$$\vec{\omega} = \omega \vec{e}_z = \frac{\vec{r} \times \vec{v}}{|\vec{r}|^2} = \frac{v}{|\vec{r}|} \vec{e}_z, \tag{1}$$

where $\vec{r} = l \sin\gamma \, \vec{e}_x + l \cos\gamma \, \vec{e}_y$ and $\vec{v}$ identify current position and axial velocity of the load of mass m, respectively. Equation 1 reveals the proportionality between $\omega = -d\gamma/dt$ and v, which also share the same polarity according to $\omega = v/|\vec{r}|$. It is instructive to observe that, under $\gamma \in [0, \pi]$, when the pendulum descends (ascends) both ω and v are negative[**] (positive). Thus, as the pendulum descends rotating clockwise (counterclockwise) under $\gamma \in [0, \pi]$ ($\gamma \in [-\pi, 0]$), the load axial velocity v, here a rate of descent, is negative (positive). The significance of this observation lies in the fact that the signal processed over a sense phase is typically proportional to the load rate of descent. As a result, the sign-inverted integral of the processed signal at the end of the sense phase is a net positive (negative) voltage, which may be applied as DC stimulus to the armature node in the drive phase, thus leading to the emergence of a motor torque with positive (negative) M under $\gamma \in [0, \pi]$ ($\gamma \in [-\pi, 0]$).

One of the external torques acting on the load at all times, and thus included in Figure 1(b) and (c), is due to the gravitation force $\vec{F_L} = -m \cdot g \cdot \vec{e}_y$ and is expressed by

$$\vec{M}_{\mathrm{L}} = \vec{r} \times \vec{F_L} = M_{\mathrm{L}} \cdot \vec{e}_z, \tag{2}$$

where

$$M_{\mathrm{L}} = -m \cdot g \cdot l \cdot \sin\gamma. \tag{3}$$

Note that M_{L} is negative (positive) under $\gamma \in [0, \pi]$ ($\gamma \in [-\pi, 0]$). The other external torque, counteracting the pendulum movement both in its natural gravitation-induced descent over a sense phase and in its motor-driven ascent in the course of a drive phase, as shown in Figure 1(b) and (c), is due to friction and may be described as

$$\vec{M}_{\mathrm{F}} = M_{\mathrm{F}} \cdot \vec{e}_z, \tag{4}$$

in which

$$M_{\mathrm{F}} = -B_m \cdot \omega, \tag{5}$$

with B_m denoting the positive-valued friction coefficient. It is instructive to point out that, under $\gamma \in [0, \pi]$, M_{F} is positive (negative) during the pendulum descent (ascent).[††] Importantly, the motor torque $\vec{M}$, acting on the load only in the drive phase, as illustrated in Figure 1(c), is expressed by

$$\vec{M} = M \cdot \vec{e}_z, \tag{6}$$

where

$$M = c \cdot \varphi \cdot i_{\mathrm{A}}, \tag{7}$$

with c representing the positive dimensionless motor constant. Observe that, under $\gamma \in [0, \pi]$ ($\gamma \in [-\pi, 0]$), M is always positive (negative) over a drive phase, resulting in a motor torque $\vec{M}$ counteracting

[**]The common sign of ω and v is opposite for both descent and ascent cases under $\gamma \in [-\pi, 0]$.
[††]The sign of M_F is opposite for both descent and ascent cases under $\gamma \in [-\pi, 0]$.

DOI: 10.1002/cta

the action of the gravitation torque $\vec{M}_{\mathrm{L}}$. As mentioned earlier, this is because, during a drive phase, the armature current i_{A} is always positive (negative) for $\gamma \in [0, \pi]$ ($\gamma \in [-\pi, 0]$), given the negative feedback action of the CSL control circuitry, that, in the preceding sense phase, typically integrates and inverts the sign of a negative (positive) rate of descent, thus providing a net positive (negative) DC voltage at the output of the inverting integrator at the end of the sensing operation, ready to be applied as DC stimulus to the armature node in the next drive phase.

The moment of inertia J of a joint-limb structure is given by

$$J = J_{\mathrm{motor}} + J_{\mathrm{limb}},$$

where the first contribution is the moment of inertia of the motor, while the second one, expressed by $J_{\mathrm{limb}} = m \cdot l^2$, denotes the limb moment of inertia. We further define $\vec{M}_{\mathrm{sum}} = \vec{M}_{\mathrm{L}} + \vec{M}_{\mathrm{F}} + \vec{M}$ as the total load torque, where $\vec{M}$ is only active in the drive phase (note that M_{L}, M_{F} and M are signed real values). Given that the electromotive force v_{ind} falling across the motor terminals is proportional to the pendulum angular velocity [34] according to

$$v_{\mathrm{ind}} = c \cdot \varphi \cdot \omega, \tag{8}$$

taking into account the differential equation governing the time evolution of γ, applying Newton's law for rotatory motion to the inverted pendulum system (using Eqns 3, 5 and 7) and imposing the satisfaction of the KVL to the mesh identified by the circuit topology of the rotor stage in Figure 2(b), the equations of the electromechanical model of the motor-pendulum structure under DC excitation of the armature node A are found to be

$$\frac{d\gamma}{dt} = -\omega, \tag{9}$$

$$\frac{d\vec{\omega}}{dt} = \frac{1}{J} \cdot \vec{M}_{\mathrm{sum}}, \quad \rightarrow \quad \frac{d\,\omega}{dt} = \frac{1}{J} \cdot \left(-m \cdot g \cdot l \cdot \sin\gamma - B_{\mathrm{m}} \cdot \omega + c \cdot \varphi \cdot i_{\mathrm{A}}\right), \tag{10}$$

$$\frac{di_{\mathrm{A}}}{dt} = \frac{1}{L_{\mathrm{A}}} v_{\mathrm{A}} - \frac{1}{L_{\mathrm{A}}} \cdot R_{\mathrm{A}} \cdot i_{\mathrm{A}} - \frac{1}{L_{\mathrm{A}}} \cdot c \cdot \varphi \cdot \omega. \tag{11}$$

Equations 9–11 represent a third-order non-autonomous dynamic system with input $v_{\mathrm{A}} \in \mathbb{R}$ and states $\gamma \in \mathbb{R}$, $\omega \in \mathbb{R}$ and $i_{\mathrm{A}} \in \mathbb{R}$. In the sense phase of the GAF paradigm, the armature current is null; thus, the loaded rod is left free to rotate autonomously. As a result, the inverted pendulum structure reduces to an autonomous second-order system constituted by Eqns 9 and 10 with $i_{\mathrm{A}} = 0$ A (here, the armature voltage is only sensed by means of the relation $v_{\mathrm{A}} = v_{\mathrm{ind}} = c\,\varphi\,\omega$).

Looking back to the block diagram of the classical GAF paradigm (Figure 2(a)), let t_0 denote the initial time of a sensing operation, running for a time interval $\Delta t_{\mathrm{sense}}$. During this phase, the switch S_{gaf} is kept in the configuration shown in Figure 2(a), allowing a sign-inverting time integration of the armature voltage v_{A} to provide the following voltage signal at the output node of the integrator

$$v_{\mathrm{int1}}(t) = v_{\mathrm{int1}}(t_0) - K_{\mathrm{int1}} \int_{t_0}^{t} v_{\mathrm{ind}}\,(t')dt' \quad \text{for} \quad t \in [t_0, t_0 + \Delta t_{\mathrm{sense}}], \tag{12}$$

where

$$v_{\mathrm{int1}}(t_0) = v_{\mathrm{int1}}(t_{\mathrm{i}}) - K_{\mathrm{int1}} \int_{t_{\mathrm{i}}}^{t_0} v_{\mathrm{ind}}\,(t')dt', \tag{13}$$

with t_{i} denoting the initial time of the control paradigm application (note that we always set $v_{\mathrm{int1}}(t_{\mathrm{i}}) = 0$ V), and we used the algebraic constraint $v_{\mathrm{A}}(t) = v_{\mathrm{ind}}\,(t)$, holding over the time interval under consideration, because no current flows through the rotor stage (i.e. $i_{\mathrm{A}} = 0$ A), while K_{int1} represents a positive coefficient inversely proportional to the integrator time constant and thus having s^{-1} as unit. It

DOI: 10.1002/cta

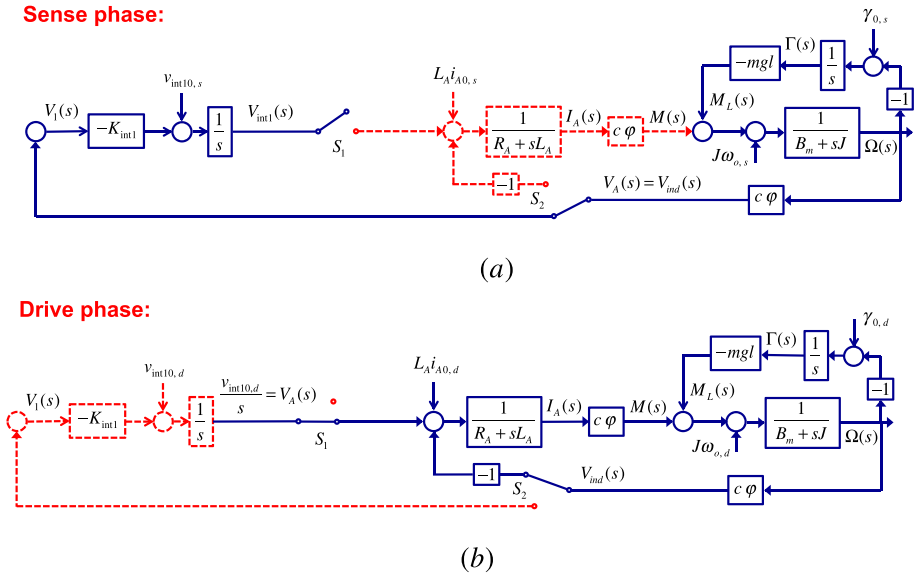

Figure 3. Block diagram of the overall dynamic system, consisting of the Go-Against-the-Force cognitive sensorimotor loop-controlled motor-pendulum structure, according to its Laplace domain representation over the course of a sense phase (a) or drive phase (b) under the assumption $\gamma \approx \bar{\gamma} = 0$. In order to better highlight the active blocks for each phase, the inactive paths are not shown in the diagrams. The large circles represent summers. Importantly, the inactive parts in each phase are marked in dotted line style and red colour. [Colour figure can be viewed at wileyonlinelibrary.com]

is instructive to note that, despite, as mentioned earlier, over a sense phase the inverted pendulum system may be described simply by an autonomous second-order system, as defined by Eqns 9 and 10, the integration operator in the GAF control loop adds a new degree of freedom, so, effectively, the overall dynamic system is a third-order autonomous system here. During the subsequent drive phase, covering a time interval Δt_{drive} , the switch S_{gaf} of Figure 2(a) is maintained in the complementary mode, driving the armature node A (Figure 2(b)) with a constant signal equal to the value of the integrator output voltage at the end of the preceding sense phase, that is,

$$\begin{aligned} v_{\text{A}}(t) &= v_{\text{int1}}(t_0 + \Delta t_{\text{sense}}) \\ &= v_{\text{int1}}(t_0) - K_{\text{int1}} \int_{t_0}^{t_0+\Delta t_{\text{sense}}} v_{\text{ind}}\,(t')dt' \quad \text{for} \quad t \in [t_0 + \Delta t_{\text{sense}}\,, t_0 + \Delta t_{\text{sense}} + \Delta t_{\text{drive}}], \end{aligned} \tag{14}$$

which, as should be clear by now, leads to the pendulum ascent thanks to the negative feedback action of the CSL control loop. The original control approach is based upon a consecutive series of sensing and driving operations of this kind, which progressively set the pendulum to the upright position. As pointed out earlier, the name 'Go-Against-the-Force' attributed to this paradigm reflects the 'work' of the motor torque $\vec{M}$, acting on the load over the drive phases, which aims at counteracting the effects of the gravitation torque $\vec{M}_{\text{L}}$. More details on the GAF control technique will be revealed in Section 2.2 during the description of the LTSpice simulations on its circuit implementation, to be presented in Section 2.1.

In order to gain some further insights into the operation of the system under control, it may be instructive to derive its Laplace domain representation. As it is standard in the literature, a capital letter shall be used to indicate the Laplace transform of a signal. For the sake of simplicity, in the presentation of the Laplace domain model of the overall dynamic system, consisting of the inverted pendulum controlled by the feedback loop,[‡‡] we assume that the angle γ is very close to the unstable

[‡‡]The assumption $\gamma \approx \bar{\gamma} = 0$ is considered only for the derivation of the Laplace domain representation of the system under control, while no constraint on the angle values is imposed later in the numerical analysis of the original CSL-controlled motor-pendulum structure.

DOI: 10.1002/cta

equilibrium[§§] $\bar{\gamma} = 0$; thus, $\sin\gamma \approx \gamma$, that is, only small perturbations around the pendulum upright position are allowed. Letting $\gamma(t_0) = \gamma_{0,s}\,(\gamma(t_0 + \Delta t_{\text{sense}}) = \gamma_{0,d})$, $\omega(t_0) = \omega_{0,s}\,(\omega(t_0 + \Delta t_{\text{sense}}) = \omega_{0,d})$ and $i_A(t_0) = i_{A0,s}\,(i_A(t_0 + \Delta t_{\text{sense}}) = i_{A0,d})$, with t_0 denoting the initial time of a sense phase and Δt_{sense} its time duration, the Laplace domain representation of the overall dynamic system, expressed by Eqns 9–11 for the motor-pendulum structure and by Eqns 12 and 14 for the CSL circuitry, may be shown in a compact form in Figure 3(a) and (b) for the sense (drive) phase. For each phase, the inactive paths are kept in the block diagram but highlighted in dotted line style and red colour. In these plots, switches S_1 and S_2 change operation mode simultaneously, realising the functionality of the single switch shown in the general block diagram of the GAF control strategy, presented earlier in Figure 2(a). Regarding the sense phase, when, looking at Figure 3(a), S_1 is clicked into its upper position decoupling the output of the inverting integrator from the motor input stage, while S_2 connects the armature node A to the input of the inverting integrator, thus yielding $i_A = 0$ A, transforming Eqns 9 and 10 in the Laplace domain, the electromotive force $V_{\text{ind}}(s)$, identically equal to the armature voltage $V_A(s)$ (here, Eqn 11 is not part of the model), is sensed as specified in the formula

$$V_{\text{ind}}(s) = c \cdot \varphi \cdot \Omega(s), \tag{15}$$

where

$$\Omega(s) = \left(s + \frac{B_m}{J} - \frac{m \cdot g \cdot l}{J \cdot s}\right)^{-1} \cdot \left(\omega_{0,s} - \frac{m \cdot g \cdot l}{J \cdot s} \cdot \gamma_{0,s}\right), \tag{16}$$

and integrated with negative sign according to the expression

$$V_{\text{int1}}(s) = \frac{v_{\text{int10,s}}}{s} - \frac{K_{\text{int1}}}{s} V_{\text{ind}}(s), \tag{17}$$

descending from Eqn 12 with the initial condition of the integrator output voltage defined as $v_{\text{int1}}(t_0) = v_{\text{int10,s}}$. With reference to the drive phase, when, with reference to Figure 3(b), switch S_1 is configured into its lower position, while switch S_2 breaks the inverting integrator path, mapping Eqns 9–11 in the Laplace domain, the application of the result of the inverting integration of the electromotive force at the end of the preceding sense phase to the armature node A, that is, letting $V_A(s) = v_{\text{int10,d}}/s$, as follows from the Laplace domain representation of Eqn 14 after defining

$$v_{\text{int10,d}} = v_{\text{int1}}(t_0 + \Delta t_{\text{sense}}), \tag{18}$$

the pendulum angular velocity $\Omega(s)$ is bound to evolve as governed by the following equation:

$$\begin{aligned}\Omega(s) = &\left(s + \frac{B_m}{J} - \frac{m \cdot g \cdot l}{J \cdot s} + \frac{(c \cdot \varphi)^2}{J \cdot (R_A + s \cdot L_A)}\right)^{-1} \\ &\cdot \left(\omega_{0,d} - \frac{m \cdot g \cdot l \cdot \gamma_{0,d}}{J \cdot s} + \frac{c \cdot \varphi}{J \cdot s \cdot (R_A + s \cdot L_A)} \cdot v_{\text{int10,d}} + \frac{c \cdot \varphi \cdot L_A \cdot i_{A0,d}}{J \cdot (R_A + s \cdot L_A)}\right),\end{aligned} \tag{19}$$

where $i_{A0,d} = 0$ A. Because of the negative sign in front of the sign of integration in the expression for $v_{\text{int1}}(t_0 + \Delta t_{\text{sense}})$ (Eqn 14), the motor is eventually induced to rotate in the opposite direction with respect to its motion at the end of the previous sense phase, leading inevitably to the pendulum ascent. It may be shown that, taking the Laplace transforms of the expressions for $\Omega(s)$ in the sense and drive phases, that is, Eqns 16 and 19, respectively, choosing appropriate initial conditions for the GAF paradigm (details are provided later) except for the starting value for γ, chosen here pretty close to the unstable state to satisfy the small-angle approximation, the resulting time waveform for ω undergoes small oscillations around the null value, as expected from the stabilising action of the control paradigm, and confirmed

[§§] More precisely, the equilibria of the dynamic system defined by Eqns 9–11 are $(\bar{\gamma}, \bar{\omega}, \bar{i}_A) \in \{(0,0,0), (\pi,0,0)\}$. The first equilibrium is unstable, while the latter is stable (recall that γ is defined as the angle between the unit vector $\vec{e}_y$ and the position vector $\vec{r}$).

DOI: 10.1002/cta

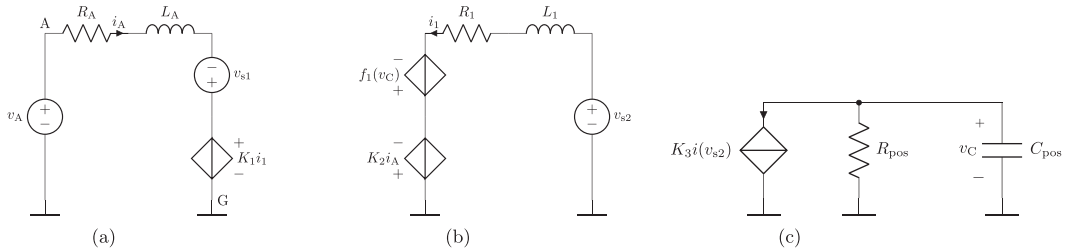

Figure 4. Circuit-theoretic implementation of the electromechanical model of the motor-pendulum system of Figure 2(b). Plot (a) realises the electrical part of the rotor stage. The circuit for the mechanical part of the rotor stage as well as for the loaded rod attached to the motor is reproduced in plot (b). (c) Circuit for the calculation of the pendulum angular position.

in LTSpice simulations of a circuit-theoretic model of the controlled motor-pendulum system (see later for details).

2.1. Circuit-theoretic implementation of the motor-pendulum system under Go-Against-the-Force cognitive sensorimotor loop control

We are now ready to introduce a circuit[¶¶] modelling the application of the GAF control strategy to the motor-pendulum system, as illustrated in the block diagram of Figure 2(a). First, Figure 4 shows the circuit realisation of the electromechanical model of the motor-pendulum system shown in Figure 2(b). Applying the KVL to the one-mesh circuit in plot (a) of Figure 4, referring to the electrical part of the rotor stage shown in Figure 2(b), one may obtain Eqn 11 provided the current i_1 is proportional to the pendulum angular velocity ω according to[‖‖] $i_1 = k_{\text{conv},1} \cdot \omega$, with $k_{\text{conv},1} = 1$ A s, $K_1 = k_{\text{conv},2} \cdot c \cdot \varphi$ is a constant with unit V A^{-1} ($k_{\text{conv},2} = 1$ A s^{-1}) and $v_{s1} = 0$ V (the only function of this source is to measure the armature current i_A). Note that the voltage across the controlled source represents the electromotive force falling across the motor in response to its rotation. Importantly, A and G in plot (a) respectively denote armature and ground node.

The application of the KVL to the one-mesh circuit in plot (b) of Figure 4, modelling the mechanical part of the rotor stage of Figure 2(b) as well as the loaded rod connected to the motor, results in Eqn 10 under the provision that L_1 is proportional to the moment of inertia J of the motor-pendulum system according to $L_1 = k_{\text{conv},3} \cdot J$ with $k_{\text{conv},3} = 1$ A^{-2} s^{-2}, $K_2 = k_{\text{conv},4} \cdot c \cdot \varphi$ is a constant with unit V A^{-1}, $k_{\text{conv},4}$ a coefficient with nominal unitary value measured in A^{-1} s^{-1}, $R_1 = k_{\text{conv},5} \cdot B_m$, with $k_{\text{conv},5} = 1\,\Omega$ s kg^{-1} m^{-2}, $v_{s2} = 0$ V (this voltage source is merely used for sensing the current i_1), and, finally, $f_1(v_C) = -m \cdot g \cdot l \cdot \sin(k_{\text{conv},6} \cdot v_C) \cdot k_{\text{conv},7}$, where $k_{\text{conv},6} = 1$ V^{-1}, while $k_{\text{conv},7} = 1$ V s^2 kg^{-1} m^{-2}. Observe that v_C models the pendulum angular position according to $v_C = k_{\text{conv},6}^{-1} \cdot \gamma$, the upper (lower) controlled source accounts for the gravitation (motor) torque acting on the load, while the linear resistor captures the effects of the friction torque counteracting the rod motion at all times.

The circuit in Figure 4(c) is used to compute the time integral of the pendulum angular velocity ω, allowing the derivation of the angle γ between the rod and the unit vector $\vec{e}_y$. In fact, this circuit implements Eqn 9, provided the controlled source generates a current proportional to the pendulum angular velocity according to $i(v_{s2}) = i_1$, K_3 is a dimensionless parameter with nominal unitary value and capacitor C_{pos} is set to 1 F. Here, R_{pos} is a very large resistor used to prevent convergence issues in the LTSpice simulations described in Section 2.2. The motor under study is endowed with a gear reduction ratio 22:1. Thus, as compared with the nominal case of a motor with no gear reduction ratio [47], here, the evolution rate of the pendulum angle γ (the motor torque M) is reduced (increased)

[¶¶] Despite, for simplicity of exposition, the circuit realisation of the electromechanical model of the original CSL-controlled inverted pendulum presented here adopts controlled sources, an equivalent operational amplifier-based implementation with supply levels 0 and 9 V was also employed to evaluate the performance of the GAF control strategy investigated in this part I paper.

[‖‖] The unit conversion constants $k_{\text{conv,j}}$ with $j \in \{1, 2, 3, 4, 5, 6, 7\}$ are introduced to properly adjust the units of measurement of addends in the equations of circuits in plots (a), (b) and (c) of Figure 4.

DOI: 10.1002/cta

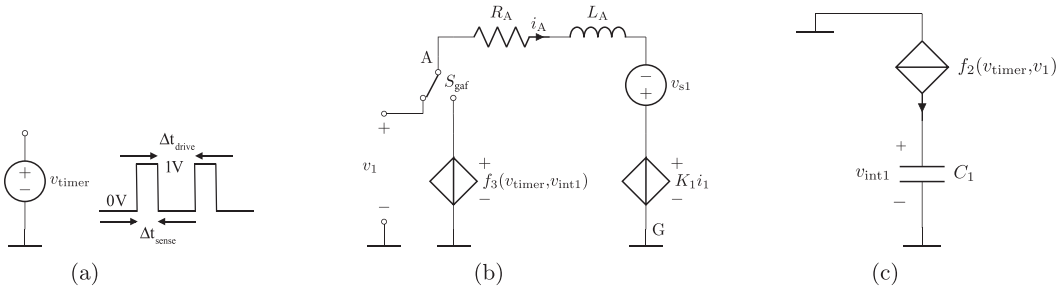

Figure 5. Circuit theoretic implementation of the electrical part of the rotor stage under Go-Against-the-Force control. (a) A voltage source v_{timer} generates a square waveform – in the inset – controlling the operation of the circuits in plots (b) and (c), particularly the operating modes of the switch S_{gaf} as well as of the two controlled sources $f_2(\cdot,\cdot)$ and $f_3(\cdot,\cdot)$. (b) Armature circuit endowed with a switch, referred to as S_{gaf}, coupling the voltage at the armature node A to the input of the inverting integrator, over the course of a sense phase, or constraining v_{A} to follow the direct current voltage v_{int1} over a drive phase. The current-controlled voltage source $K_1 i_1$ accounts for the electromotive force across the motor terminals. (c) Circuit implementing the inverting integration of the armature voltage over a sense phase.

by a factor 22. Thus, looking at the circuit of Figure 4(c), realising the differential equation relating pendulum angular velocity ω to pendulum angle γ, the dimensionless coefficient K_3 is chosen as $1/22 = 4.55 \cdot 10^{-2}$. Further, with reference to the circuit of Figure 4(b), implementing Newton's law for rotatory motion, the numerical value for $k_{\text{conv},4}$, appearing in the expression for K_2, is set to 22.

The implementation of the sensing and driving operations of the GAF control system requires the modification of the circuit of Figure 4(a), modelling the electrical part of the rotor stage, to allow the inclusion of an ad hoc closed-loop control system.

The modified circuit, shown in Figure 5, allows to sample the voltage of the armature node A over a sense phase, or to apply a DC voltage to this same node during a drive phase. The voltage source v_{timer} is used to generate a periodic square waveform of amplitude 1 V over the course of a Δt_{sense}-long sense phase and 0 V during the subsequent Δt_{drive}-long drive phase (Figure 5(a)). When $v_{\text{timer}} > 0.5$ V, that is, over the course of a sense phase, the switch S_{gaf} in Figure 5(b) is kept in the shown configuration, allowing to couple the node at voltage v_{A} to the input of the inverting integrator. Concurrently, the voltage $v_1 = K_1 \cdot i_1$ is integrated through the insertion of a current generated by the voltage-controlled current source $f_2(v_{\text{timer}}, v_1)$, defined as

$$f_2(v_{\text{timer}}, v_1) = \begin{cases} -v_1/R_2 & \text{if} \quad v_{\text{timer}} > 0.5 \text{ V}, \\ 0\,A & \text{if} \quad v_{\text{timer}} \leq 0.5 \text{ V}, \end{cases} \tag{20}$$

into a capacitor – here called C_1 – as shown in Figure 5(c) (with reference to Figure 3(a), the expression for the integration constant is then $K_{\text{int1}} = 1/(R_2 \cdot C_1)$). When $v_{\text{timer}} \leq 0.5$ V, that is, over the course of a drive phase, the integrator stops working (the controlled current source in Figure 5(c) drives no current into the capacitor), while the switch S_{gaf} in Figure 5(b) assumes the complementary configuration, connecting the top terminal of the voltage-controlled voltage source $f_3(v_{\text{timer}}, v_{\text{int1}})$, generating the signal

$$f_3(v_{\text{timer}}, v_{\text{int1}}) = \begin{cases} 0\,\text{V} & \text{if} \quad v_{\text{timer}} > 0.5 \text{ V}, \\ v_{\text{int1}} & \text{if} \quad v_{\text{timer}} \leq 0.5 \text{ V}, \end{cases} \tag{21}$$

to the node at voltage v_A, which is then set to the DC voltage appearing at the integrator output at the end of the preceding sense phase (note that during the sensing operation, that is, for $v_{\text{timer}} > 0.5$ V, the voltage value of $f_3(v_{\text{timer}}, v_{\text{int1}})$, here set to 0 V, has no impact on the armature node, because, as mentioned earlier, the switch S_{gaf} couples the latter to the node at voltage v_1).

All in all, the circuit-theoretic model for the motor-pendulum system under GAF CSL control combines the circuits of Figures 4(b) and (c) and 5. Table I gives numerical values and units for all parameters of these circuits. The particular motor under consideration in this research is identified by the code 2619S012SR 22:1 and is fabricated from Faulhaber [48]. The values for parameters R_{A}, L_{A},

DOI: 10.1002/cta

Table I. Parameters of the circuits of Figures 4(b) and (c) and 5 for the LTSpice simulations discussed in Section 2.2.

Parameter	Value	Parameter	Value
m	10 g	l	10 cm
R_A	36.5 Ω	L_A	2.2 mH
K_1	19.1 mV·A^{-1}	K_2	0.42 V·A^{-1}
R_1	1 μΩ	v_{sj}, $j \in \{1,2\}$	0 V
L_1	100 μH	K_3	$4.55 \cdot 10^{-2}$
R_2	330 kΩ	C_1	10 nF
C_{pos}	1 F	R_{pos}	1 MΩ
Δt_{sense}	1 ms	Δt_{drive}	9 ms

$J_{motor} = 68 \cdot 10^{-9}$ kg m^2 << $J_{limb} = m \cdot l^2 = 10 \cdot 10^{-3}$ kg $\cdot(10 \cdot 10^{-2}$ m$)^2 = 10^{-4}$ kg m^2. With reference to Figure 3(a), $K_{int1} = 1/(R_2 \cdot C_1) = 303\,s^{-1}$. In the simulation of Figure 7, the values for m, Δt_{sense} and Δt_{drive} shall be modified for visualisation purposes.

J_{motor}, c and φ, used in the LTSpice simulations to follow, have been extracted from the data sheet of this motor. This sheet reports no information about the friction coefficient B_m. As a result, the selection for the resistance of the linear resistor R_1 was based upon a standard value for B_m, specifically 10^{-6} kg m^2 s^{-1}. The values for C_1 and R_2 were chosen as in the design of a hardware circuit realisation of the motor-pendulum system under GAF CSL control, which was fabricated in house (see Appendix A for details) to confirm the accuracy of the LTSpice simulation results presented in Section 2.2.

2.2. *LTSpice simulations of the circuit theoretic model of the motor-pendulum system under Go-Against-the-Force cognitive sensorimotor loop control*

With reference to the circuitry in Figures 4(b) and (c) and 5, modelling the overall dynamic system, the states in the Eqns 9–11 of the motor-pendulum system, that is, γ, ω and i_A, are respectively modelled by the voltage v_C across capacitor C_{pos} in Figure 4(c), the current i_1 flowing through the resistor R_1 in Figure 4(b) and the current i_A flowing through the resistor R_A in Figure 5(b). Furthermore, the integrator output voltage v_{int1}, introducing a new state variable in the sense phase, is modelled by the voltage v_{int1} across capacitor C_1 in Figure 5(c). A numerical simulation of the circuit model of the motor-pendulum system under GAF control, with initial time t_i taken as 0 s, and for initial conditions $v_C(t_i) = 3.04$ V, $i_1(t_i) = 0$ A and $i_A(t_i) = 0$ A (as mentioned earlier, at the beginning of the control strategy application, $v_{int1}(t_i)$ is always chosen as 0 V), is shown in Figure 6. Plots (a) and (b) respectively show the time evolution of the integrator output voltage v_{int1} and of the angle γ the pendulum forms with the unit vector $\vec{e}_y$.

Let us gain some further insights into the dynamics of the controlled system. As the pendulum moves back towards the stable rest position in the first sense phase, the angular velocity, and, consequently, the armature voltage, now coincident with the electromotive force, keep negative as they grow in modulus. Because the gravitation torque M_L, reported in Eqn 3, is small when γ is close to $\pi \approx 3.14$, in this first sense phase, the modulus of the pendulum angular velocity rate (i.e. of $d\omega/dt = 1/J \cdot (M_L - M_F)$, as defined in Eqn 10) keeps limited, and, as a result, the angle γ gets only a little bit larger than its initial condition, while the angular velocity and armature voltage moduli remain relatively small, leading barely to a slight increase in the integrator output voltage. In the subsequent drive phase, a modest constant voltage equal to the value for v_{int1} at the end of the sense phase is applied to the armature node A, leading to the flow of a small positive current i_A, which results into a motor torque M winning slightly over the algebraic sum of the other torques,[***] thus allowing the angle γ to undergo a little decrease.

In all subsequent sensing operations, until the pendulum attains the upright position, γ goes through a further reduction (consequently angular velocity and armature voltage assume positive values, whereas

[***] At the very beginning of a drive phase, the pendulum moves downwards; thus, the friction favours the motor torque action against gravitation. However, as the pendulum reverses motion direction, the friction torque aligns with the gravitation torque, and the motor 'work' has to counteract the action of both the other two torques.

DOI: 10.1002/cta

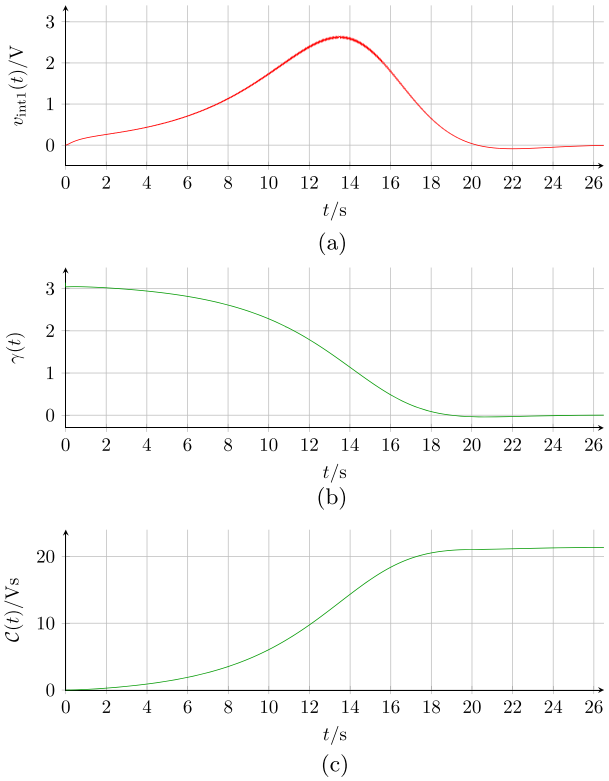

Figure 6. Application of the original Go-Against-the-Force control paradigm to the motor-pendulum system through a LTSpice simulation of the circuitry of Figures 4(b) and (c) and 5. Time evolution of the voltage v_{int1} (a), of the angle $\gamma = k_{\mathrm{conv,6}}\, v_{\mathrm{C}}$ ($k_{\mathrm{conv,6}} = 1\ \mathrm{V}^{-1}$) (b) and of the cost function $\mathcal{C}$ (c). As mentioned in the text, $v_{\mathrm{C}}(t_{\mathrm{i}}) = 3.04$ V, that is, $\gamma(t_{\mathrm{i}}) = 3.04$, $i_1(t_{\mathrm{i}}) = 0$ A and $i_{\mathrm{A}}(t_{\mathrm{i}}) = 0$ A with $t_{\mathrm{i}} = 0$ s (the initial value of the integrator output voltage, that is, $v_{\mathrm{int1}}(t_{\mathrm{i}})$, is fixed to 0 V). The value for γ_{th} used in the measurement of the time interval $\Delta t = t|_{\gamma=\gamma_{\mathrm{th}}} - t|_{\gamma=\gamma(t_{\mathrm{i}})}$ the control system needs to lift the pendulum from the initial angular position up to the threshold angle itself is set to 0.1 (note that $t|_{\gamma=\gamma(t_{\mathrm{i}})} \equiv t_{\mathrm{i}}$). The set of values for all parameters in the circuit theoretic model of the overall dynamic system is reported in Table I. Particularly, the inverted pendulum load has mass $m = 10$ g, accounted for in the expression of the voltage-controlled voltage source $f_1(v_{\mathrm{C}})$ (Figure 4(b)). [Colour figure can be viewed at wileyonlinelibrary.com]

the integrator output voltage decreases) for a while, before the gravitation and friction torques jointly nullify the pendulum ascending impetus, leading to its inevitable descent thereafter, with a consequent polarity change in angular velocity, armature voltage and integrator output, as explained earlier. Despite the non-monotonous behaviour of the time waveform of the armature voltage, as long as γ keeps below the value of $\pi/2 \approx 1.57$, the total area below this waveform over a $\Delta t_{\mathrm{sense}}$-long period keeps negative. Consequently, the net change in the inverting integrator output voltage over a sense phase maintains its positive sign. It follows that, as γ gets closer and closer to $\pi/2$, the applied voltage at node A over a drive phase is a growing positive constant, and the motor torque counteracts better and better the algebraic sum of the other two torques, lifting the pendulum up more and more significantly.

When γ attains the value of $\pi/2$, the modulus of the gravitation torque M_{L}, the integrator output voltage v_{int1} (Figure 6(a)) as well as the modulus of the angle rate of change, that is, of $d\gamma/dt$ (Figure 6(b)), exhibit maxima. For larger values of γ until the pendulum attains the upright position, the area below the time waveform of the armature voltage over a sense phase is found to be positive, resulting in a net negative change in the integrator output voltage. Thus, while keeping a positive sign, v_{int1} experiences a progressive decrease in the course of successive sensing operations, leading to a more and more gentle pendulum ascent in the following drive phases, when v_{int1} keeps unchanged. In fact, should γ attain exactly the target value of 0, the integrator output would be null too. Of course, this never happens in practice. As the pendulum passes over the upright position, the control system operates in a complementary

DOI: 10.1002/cta

fashion, aiming at increasing the angle in an attempt to stabilise the equilibrium $\bar{\gamma} = 0$. So a small sustained oscillation of the angle γ around the unstable null value is observed thereafter.

With reference to Figure 6(b), the time interval the GAF control system necessitates to raise the pendulum from the initial condition $\gamma(t_\mathrm{i}) = 3.04$, close to the stable rest state, where $\bar{\gamma} = \pi$, to a certain threshold position γ_th, here set to 0.1, in proximity to the upright position, where $\bar{\gamma} = 0$, is found to be quite large, that is,

$$\Delta t = t|_{\gamma=\gamma_\mathrm{th}} - t|_{\gamma=\gamma(t_\mathrm{i})} = 17.8\,\mathrm{s}, \tag{22}$$

where $t|_{\gamma=\gamma(t_\mathrm{i})} \equiv t_\mathrm{i}$, which, as said earlier, is chosen as 0 s. Furthermore, the GAF control system spends a considerable amount of energy to change the angle from $\gamma(t_\mathrm{i})$ to γ_th. Let us introduce the following cost function to estimate the 'work' associated with the pendulum lift:

$$C(t) = \int_{t|_{\gamma=\gamma(t_\mathrm{i})}}^{t|_{\gamma=\gamma(t)}} |v_\mathrm{A}(t')|dt', \tag{23}$$

where $v_\mathrm{A}(t_\mathrm{i}) = 0\,\mathrm{V}$ because[†††] $\omega(t_\mathrm{i}) = 0\,\mathrm{rad{\cdot}s^{-1}}$. Plot (c) in Figure 6 shows the time evolution of this cost function for the simulation under focus. When $t = t|_{\gamma=\gamma_\mathrm{th}}$, the numerical value of the cost function expressed by Eqn 23 is found to be significant, that is,

$$C(t|_{\gamma=\gamma_\mathrm{th}}) = \int_{t|_{\gamma=\gamma(t_\mathrm{i})}}^{t|_{\gamma=\gamma_\mathrm{th}}} |v_\mathrm{A}(t')|dt' = 20.4\,\mathrm{V\,s}. \tag{24}$$

The following section introduces a novel memristor-based strategy, which enables a considerable reduction in Δt and $C(t|_{\gamma=\gamma_\mathrm{th}})$, leading to a substantial improvement in pendulum lift speed with a further enviable decrease in power consumption. Before introducing the new strategy, which will further endow the control system with the capability to adapt to changes in the rod load, let us gain a deeper understanding of the dynamics of some variables of interest under the application of the original GAF paradigm to the motor-pendulum system.

Figure 7 shows clearly the operation of the GAF control system over a few successive sense and drive phases. In order to improve the quality of visualisation, in this simulation, we chose different values for the load mass m and for the time intervals of a sense phase Δt_sense and of a drive phase Δt_drive (see the figure caption for details). The time evolution of pendulum angular velocity ω, motor voltage v_ind, integrator output v_int1 and pendulum angle γ, shown in plots (a), (b), (c) and (d) for initial conditions $v_\mathrm{C}(t_\mathrm{i}) = 1.64\,\mathrm{V}$, $i_1(t_\mathrm{i}) = 0\,\mathrm{A}$, $i_\mathrm{A}(t_\mathrm{i}) = 0\,\mathrm{A}$ and $v_\mathrm{int1}(t_\mathrm{i}) = 0\,\mathrm{V}$, with $t_\mathrm{i} = 0\,\mathrm{s}$, agrees well with the theoretical predictions. As clear from plot (d), the angle γ is almost half way between stable and unstable position, that is, is about to go through the value of $\pi/2$. As explained earlier, over each sense phase shown in Figure 7, the pendulum rises a bit, driven by the momentum gained in the previous drive phase, before heading down because of gravitation. It follows that the angular velocity, and, consequently, the electromotive force keep positive for a while before decreasing towards negative values. Meanwhile, the integrator output voltage experiences an initial decrease followed by a comparable increase. Similarly, the pendulum angle initially gets smaller and then undergoes an opposite change. Over the subsequent drive phase, both angular velocity and motor voltage initially maintain their negative sign and later rise towards positive values. Meanwhile, as expected, the integrator output keeps constant (the closed-loop control system performs no integration in the drive phase), whereas the pendulum angle increases for a while and then goes through a substantial decrease.

We are now ready to introduce a novel CSL control strategy to lift a limb coupled to a joint of Myon from the stable rest state to the upright position and to stabilise it there afterwards, so as to overcome the disadvantages of the original GAF paradigm, particularly obvious from a look at the numerical values of the figures-of-merit Δt and $C(t|_{\gamma=\gamma_\mathrm{th}})$, respectively shown in Eqns 22 and 24.

[†††] The GAF control process starts always with a sense phase, and all initial conditions for pendulum angular velocity ω, armature current i_A and integrator output v_int1 are set to 0. The starting value for γ has to be set to a value different from π in the numerical simulations; otherwise, the pendulum would never leave the stable rest state, while in the actual hardware implementation (Appendix A) $\gamma(t_\mathrm{i})$ may also be chosen as π, because any tiny noise-induced perturbation of the pendulum from the stable rest state, unavoidable in practice, would lead to a successful accomplishment of the control strategy objective.

DOI: 10.1002/cta

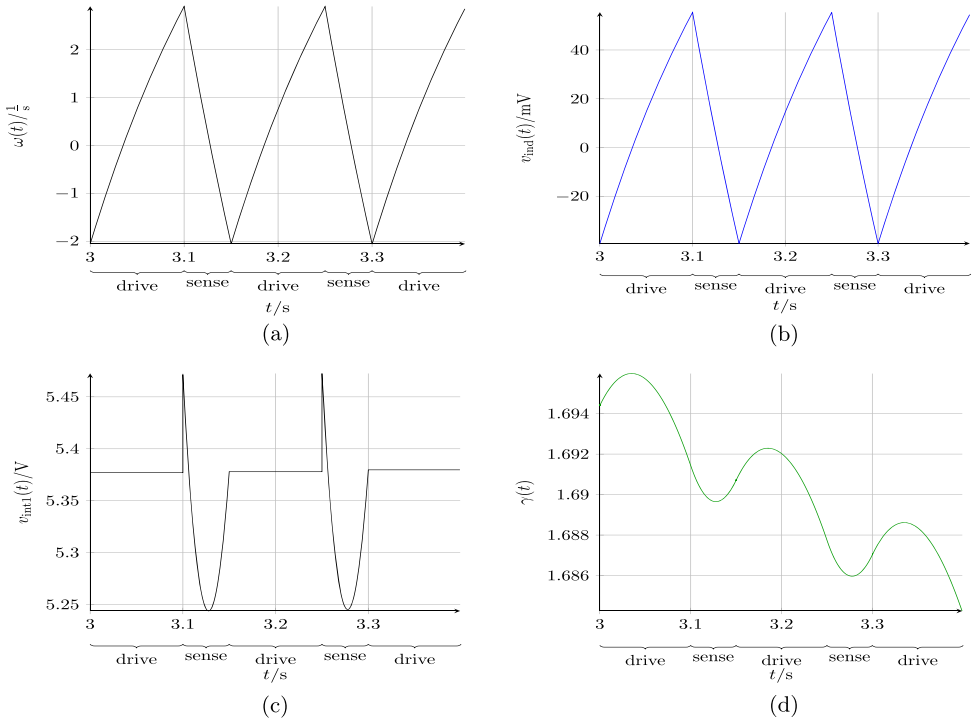

Figure 7. Further insights into the dynamics of the Go-Against-the-Force control system. Loci of ω (a), v_{ind} (b), v_{int1} (c) and γ (d) versus a time interval covering a number of consecutive sense and drive phases from a LTSpice simulation of the circuitry in Figures 4(b) and (c) and 5. Here, in the expression for $f_1(v_C)$, $m = 40$ g. Further, $\Delta t_{\text{sense}} = 50$ ms and $\Delta t_{\text{drive}} = 100$ ms, while the initial conditions are $v_C(t_i) = 1.64$ V, $i_1(t_i) = 0$ A, $i_A(t_i) = 0$ A and $v_{\text{int1}}(t_i) = 0$ V (here, $t_i = 0$ s). The inductor L_A in the armature circuit of Figure 5(b) is responsible for the appearance of spikes in the time waveform of v_{int1} in correspondence to the switching of the control system between sense and drive phases. [Colour figure can be viewed at wileyonlinelibrary.com]

3. NOVEL MEMRISTOR-CENTRED KICK-FLY-CATCH CONTROL STRATEGY

The novel memristor-centred KFC strategy proposed in this work is based upon the application of the maximum principle of Pontryagin [49] to the motor-pendulum system expressed by Eqns 9–11, which allows to derive an optimal choice for the control voltage v_{ctrl} to be applied to the armature node A so as to induce a time-efficient and energy-efficient movement of a robot's limb from the stable rest state to the upright position.[‡‡‡] In the application of Pontryagin's theory, the choice for the control voltage v_{ctrl} was optimised in terms of limb movement speed. The analytic treatment, reported in Appendix B, led to a three-phase control procedure, which clarifies the origin of the nomenclature, namely, 'Kick-Fly-Catch', adopted to refer to the proposed strategy. Figure 8(a) illustrates the block diagram model of the motor-pendulum system under the KFC strategy. During the first phase, named kick, the switch $S_{\text{kick-fly}}$ is flipped into its uppermost configuration, allowing the maximum operating DC voltage $v_{\text{ctrl}} = v_{\text{ctrl,max}}$ to be transferred to the armature node A via an impedance converter, inducing the exertion of the largest possible motor torque M_{max} on the pendulum load, which would then rapidly ascend towards the target position. The dynamics of the inverted pendulum over a kick phase are illustrated in Figure 8(b). This phase should ideally come to an end when the pendulum is pretty close to the desired unstable state. At this point, the second phase, named fly, would commence. Here, the switch $S_{\text{kick-fly}}$ in Figure 8(a) is clicked into its lowermost position; thus, no control signal is applied to the armature node, whose voltage v_A identically follows the electromotive force v_{ind} falling across the motor terminals, and the

[‡‡‡]It is noteworthy to stress that, similarly as in the original GAF paradigm, the armature node A is supposed to be driven by a certain control voltage v_{ctrl} in control mode, corresponding to a drive phase in the GAF approach, and to assume the same voltage as the electromotive force v_{ind} appearing between the motor terminals under no control, equivalent to a sense phase in the paradigm revisited in Section 2.

DOI: 10.1002/cta

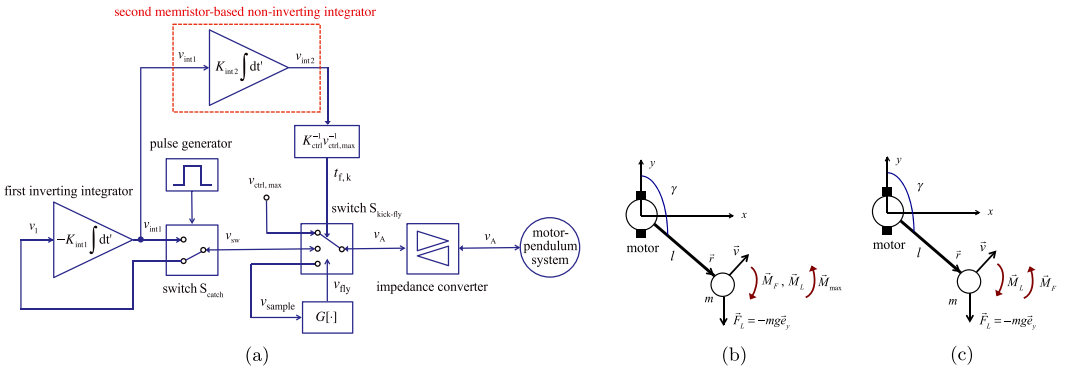

Figure 8. Block diagram representation of the of the motor-pendulum system under the proposed KFC control strategy (a). The inverted pendulum over a typical kick phase (b) and fly phase (c) under the hypothesis $\gamma \in [0, \pi]$. [Colour figure can be viewed at wileyonlinelibrary.com]

pendulum is left free to evolve autonomously towards the final destination. Only gravitation and friction torques oppose its movement, as depicted in Figure 8(c). During this phase, a nonlinear memory block with operator $G[\cdot]$ [6] (Figure 8(a)) continuously measures sign and modulus of its input voltage v_{sample}, coincident with the armature voltage v_{A}, thus indirectly monitoring the pendulum angular velocity ω, or, equivalently, the pendulum axial velocity v. As soon as the armature voltage changes sign (the pendulum ascent has come to a halt and its inevitable descent is about to start), or increases in modulus (the pendulum has gone over the upright position and has just commenced to fall from the other side of the x axis, see Figure 8(c) for reference), the nonlinear memory block in Figure 8(a) outputs a positive voltage v_{fly}, which clicks the switch $S_{\text{kick-fly}}$ into its middle position, signalling the end of the fly phase. At this point, the catch phase sets in. Here, an iterative cycle of sensing and driving operations, as defined by the standard GAF control strategy protocol, stabilises the upright position (see Figure 1(b) and (c) for a visualisation of the torques acting on the pendulum load during the sense and drive phases, respectively). With reference to Figure 8(a), the pulse generator-controlled switch S_{catch} is alternately flipped into its lower or upper configuration, respectively, allowing to sense the armature node voltage v_{A}, that is, the motor electromotive force v_{ind}, which is coincidentally integrated with negative sign by the inverting integrator (this is the sensing mode control operation), or to apply a DC voltage equal to the inverting integrator output at the end of the previous sense phase to the armature node, thus inducing a motor torque, which, acting on the pendulum mass, lifts it up counteracting successfully the gravitation and friction torques (the system operates in driving mode then). Very importantly, in the proposed KFC paradigm, the length and power-consuming sense-and-drive control procedure is applied only when the pendulum is in the neighbourhood of its final desired state, resulting in a considerable improvement in terms of time and energy efficiency over the old approach.

By inspecting the model of Figure 8(a), we may notice the presence of a second integrator, which integrates with positive sign and time constant K_{int2} the first inverting integrator output voltage v_{int1} during the catch phases (the output of the first integrator is grounded over the kick and fly phases). As explained in more detail later, this new integrating path, absent in the block diagram representation of the GAF paradigm (Figure 2(a)), allows to estimate the final time of the kick phase, denoted simply as $t_{\text{f,k}}$, from the current value of the non-inverting integrator output voltage v_{int2} (a gain block with scaling factor $K_{\text{ctrl}} \cdot v_{\text{ctrl,max}}$, where K_{ctrl} denotes a suitable positive real constant, allows the appropriate conversion of a voltage signal into a time variable). The non-inverting integrator output voltage needs to be stored securely between successive strategy applications in order to be retrieved and updated over the catch phases. These storage and updating operations, invaluable to adapt the estimation of the kick phase time duration to changes in the external conditions (e.g. modifications to the pendulum geometry), are carried out through a simple analogue electronics circuit exploiting the capability of a nonvolatile memristor to store and process data in the same physical location.

DOI: 10.1002/cta

Remark 1

The idea behind the introduction of the new integrating path arises from the empirical observation that the value of the integral v_{int2} of the first inverting integrator output v_{int1} at the end of a GAF strategy run with initial pendulum angle $\gamma(t_{\text{i}}) \approx \pi$ may be considered as an estimate for the 'work' necessary to raise the pendulum from the stable rest state to the target location. As a result, before the first application of the KFC strategy, the old GAF paradigm is run once to determine a first estimate for the pendulum lift 'work'. This is the so-called initialisation step. Because the current value for v_{int2} is stored securely until the start of a catch phase, and v_{int1} is kept equal to 0 V in the preceding kick and fly phases, the aforementioned pendulum lift 'work' estimate may be progressively updated over the catch phase of each successive application of the KFC strategy. Importantly, during a kick phase, a constant DC voltage, specifically $v_{\text{ctrl,max}}$, is applied to the armature node A; thus, its integral, scaled by a factor K_{ctrl}, increases linearly with time. Equating this linear function of time to the current pendulum lift 'work' estimate allows to the determine the final time of the current kick phase, as shown in the block diagram model of Figure 8(a). Finally, the initialisation procedure fits the 'kick' to the particular geometry of the pendulum as well as to the initial conditions of the dynamic system under control. In case of perturbations to initial conditions or modifications in the pendulum geometry, the kick phase duration, fitted to the nominal case, is no longer appropriate. This possible potential issue is addressed by the KFC control system, which, throughout a catch phase, updates the pendulum lift 'work' estimate by correcting the current value for the second non-inverting integrator output voltage v_{int2}, allowing to update the kick phase duration estimate in the following KFC strategy run.

A block diagram model for the motor-pendulum structure under the kick, fly, catch (sense mode) and catch (drive mode) phases of the innovative KFC control system is depicted in Figures 9(a) and (b) and 10(a) and (b), respectively. In these four models, all signals are represented in the Laplace domain (the first letter of their symbols is thus capitalised). Unlike the block diagram description of the motor-pendulum structure under the original GAF CSL control system (refer to plots (a) and (b) of Figure 3 for the sense and drive phase, respectively), in this block diagram model, no assumption is made on the admissible range of values for γ, that is, the small-angle assumption is removed. In the block diagram of each phase, the inactive paths are marked with a dotted line style and a red colour.

Let us gain a deeper insight into the mechanisms at the basis of the proposed control system by inspecting thoroughly Figures 9(a) and (b) and 10(a) and (b). The timing of the jth ($j \in \mathbb{N} = \{1, 2, 3, \dots\}$) run of the new control strategy is regulated as described next.[§§§]

(1) At first, the largest admissible value for the control signal v_{ctrl}, referred to as $v_{\text{ctrl,max}}$, and set to the maximum operating voltage v_{B+} in the control circuit, is applied to the armature node A for a limited time interval, specifically $t \in [t_{0,\text{k}}^{(j)}, t_{\text{f,k}}^{(j)})$, where the superscript j indicates the KFC strategy iteration number, and the starting time of this control scheme run, indicated as $t_{\text{i}}^{(j)} \triangleq t_{0,\text{k}}^{(j)}$, is reset[¶¶¶] to 0 s. This is the kick phase, aiming at inducing a significant decrease in γ, while keeping it larger than 0, ideally.[‖‖‖] The block diagram of the KFC strategy over this phase is shown in Figure 9(a), where, similarly as in Figure 3(a), switch S_1 is open, switch S_2, here endowed with one further possible configuration as compared with the diagrams of Figure 3, is clicked into the uppermost position, whereas switch S_3 imposes the maximum value of the control voltage v_{ctrl} to the armature node A, that is, here, $v_A \equiv v_{\text{ctrl,max}}$. With reference to Figure 9(a) (more details shortly), a new branch including the final result of a non-inverting integration of the inverting integrator output voltage, carried out throughout the catch phase of the previous

[§§§] Throghout this manuscript, the discussion on the KFC strategy assumes a positive-signed 'kick' control voltage $v_{\text{ctrl}} = v_{\text{ctrl,max}} \in \mathbb{R}_+$, leading to a decrease in the pendulum angular position from $\bar{\gamma} = \pi$ towards $\bar{\gamma} = 0$. A similar analysis may be applied *mutatis mutandis* to the case of a negative-signed 'kick' control voltage $v_{\text{ctrl}} = v_{\text{ctrl,min}} = -v_{\text{ctrl,max}} \in \mathbb{R}_-$, which would raise the pendulum from the negative side of the x axis (refer to Figure 8(b)), that is, from $\bar{\gamma} = -\pi$ towards $\bar{\gamma} = 0$.

[¶¶¶] For each $j \in \mathbb{N} = \{1, 2, 3, \dots\}$, the jth application of the KFC control strategy to the motor-pendulum system starts at time $t_{\text{i}}^{(j)} \triangleq t_{0,\text{k}}^{(j)} = 0$ s. The initialisation phase begins at time $t_{\text{i}}^{(0)} \triangleq t_{0,\text{g}}^{(0)}$.

[‖‖‖] In case, because of an excessively strong 'kick', the pendulum went over the upright position during the kick phase, the following fly phase would practically be skipped, and the control system would enter the catch phase directly after the completion of the kick process.

DOI: 10.1002/cta

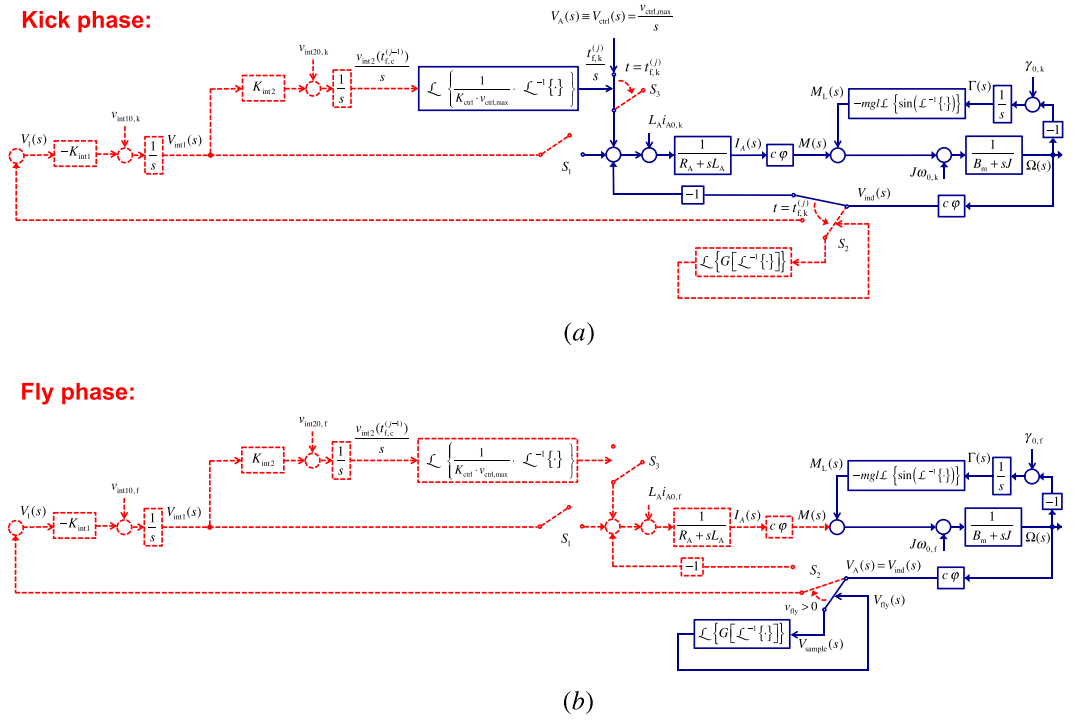

Figure 9. Block diagram model of the KFC cognitive sensorimotor loop-controlled motor-pendulum structure according to its Laplace domain representation. Here, no constraint on the range of allowable values for γ is enforced. The switches' configurations in plots (a) and (b) allow the implementation of the kick and fly phases of the paradigm. $\mathcal{L}\{\cdot\}$ denotes the Laplace operator. The inactive paths of each phase are drawn with dotted line style and red colour. [Colour figure can be viewed at wileyonlinelibrary.com]

$(j-1)$th application of the KFC strategy (for $j \in \mathbb{N} : j \neq 1$, i.e. $j \in \{2, 3, \ldots\}$) or during the run of a preliminary GAF paradigm****, the so-called initialisation phase, carried out offline previous to the first application of the KFC strategy (here, $j = 1$), dictates the time instant $t_{\mathrm{f,k}}^{(j)}$ at which the switch S_3 is opened, marking the end of the kick phase of the jth run of the proposed control scheme.††††

(2) Over the next phase, spanning a time interval $t \in [t_{0,\mathrm{f}}^{(j)}, t_{\mathrm{f,f}}^{(j)})$, with $t_{0,\mathrm{f}}^{(j)} \equiv t_{\mathrm{f,k}}^{(j)}$, the pendulum is allowed to leverage the energy gained in the previous phase to move freely towards the target position until a time instant at which either the axial velocity vector $\vec{v}$ changes direction, that is, v becomes negative – here the pendulum starts moving downwards – or its modulus $|\vec{v}| = |v|$ increases, that is, v becomes more positive – in this case, the pendulum goes over the upright position and starts its descent from the other side of the x axis (refer to Figure 8(c)). This is the fly phase, the most energy-efficient operating mode of the proposed strategy. The block diagram of the KFC paradigm in this phase is shown in Figure 9(b), where switches S_1 and S_3 are open, whereas switch S_2 is configured in the lowest position to allow an indirect observation of the pendulum axial velocity v through the monitoring of the armature voltage, here coinciding with

****The preliminary phase consists of a GAF paradigm run. Alternatively, it may be seen as a catch phase with initial conditions set as at the start of a GAF control scheme application. Further, a fictitious value is attributed to the control scheme iteration variable j in this phase, specifically 0. Taking these aspects into account, we may use the following notation to denote starting and final times of the initialisation phase, respectively, $t_i^{(0)} \triangleq t_{0,g}^{(0)}$ (which is set to 0 s) and $t_{f,g}^{(0)}$ (time at which the pendulum attains the upright position).

††††For simplicity of exposition, the superscript indicating the KFC control strategy iteration number is omitted from all variables except for those within the non-inverting integrator path, which plays a major role in the performance enhancement of the novel control strategy over the standard approach.

DOI: 10.1002/cta

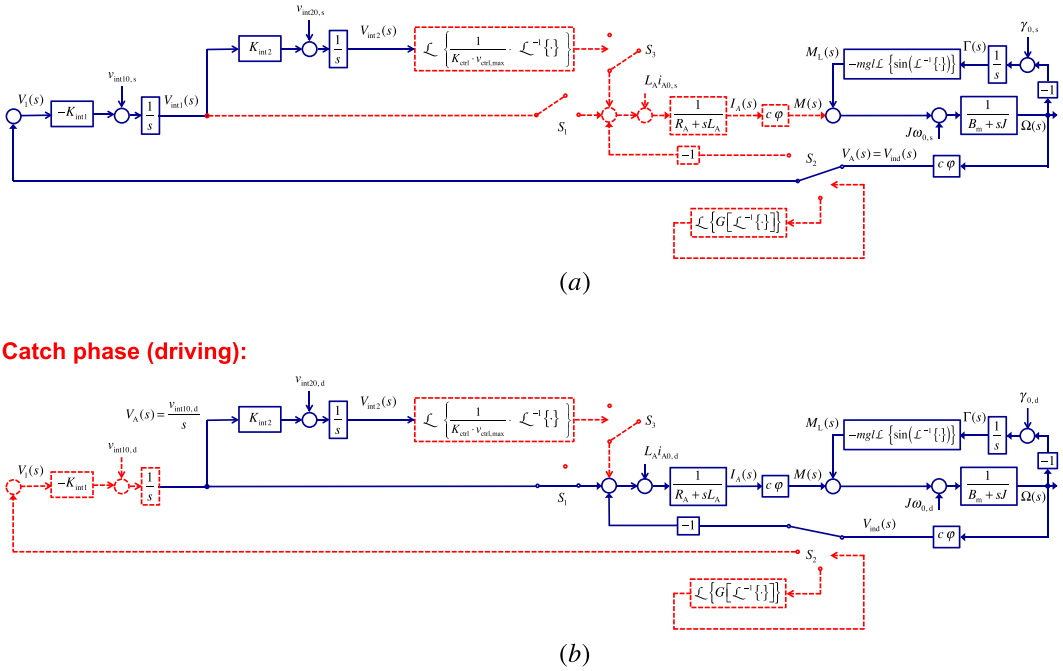

Figure 10. Block diagram model of the KFC cognitive sensorimotor loop-controlled motor-pendulum structure according to its Laplace domain representation. Here, no constraint on the range of allowable values for γ is enforced. The switches' configurations in plots (a) and (b) allow the implementation of the sense and drive operations within a catch phase of the paradigm. $\mathcal{L}\{\cdot\}$ denotes the Laplace operator. A dotted line style and a red colour are used to highlight the inactive parts for each phase. In plots (a) and (b), the switch S_2 is clicked in the uppermost (centre) configuration when the sense (drive) phase gives way to the drive (sense) phase at the end of a Δt_{sense} (Δt_{drive})-long sense (drive) mode time interval. [Colour figure can be viewed at wileyonlinelibrary.com]

the electromotive force, that is, $v_A \equiv v_{\text{ind}}$. In Figure 9(b), this monitoring action is schematically modelled through the insertion of a nonlinear memory block with operator $G[\cdot]$ [6], driven by the voltage v_{sample}, coincident with the armature node voltage v_{A} and delivering an output signal v_{fly}, which would go positive at the time $t_{\text{f,f}}^{(j)}$, where v_{A} changes sign or increases in modulus, thus disconnecting the switch S_2 from its current position and leading to the end of the jth fly phase.

(3) The original GAF paradigm is finally applied to the inverted pendulum to stabilise it in the upright position. This is the catch phase, running over a time interval $t \in [t_{\text{0,c}}^{(j)}, t_{\text{f,c}}^{(j)}]$, with $t_{\text{0,c}}^{(j)} \equiv t_{\text{f,f}}^{(j)}$ ($t_{\text{f,c}}^{(j)}$ is the last instant of the KFC control strategy application, which should last as much time as it is desirable to keep the robot limb in the upright position.[‡‡‡‡]), and consisting of a cycle of alternating sensing and driving operations, as explained earlier in Section 2. Figure 10(a) and (b) respectively refer to the block diagram of a catch phase in sense and drive mode. In plot (a), switches S_1 and S_3 are open, while switch S_2 is clicked into the centre position to allow the sensing of the armature voltage (here, $v_{\text{A}} \equiv v_{\text{ind}}$). In plot (b), switch S_1 allows to drive the armature node with the inverting integrator output voltage at the end of the preceding sense phase within the cycle of alternating sensing and driving operations within the catch phase of the jth run of the KFC control scheme, switch S_2 is set in the uppermost configuration, while switch S_3 is open. Very importantly, during the whole catch phase, a second non-inverting integrator performs the time integration of the first inverting integrator output voltage. As explained in the succeeding

[‡‡‡‡]For each $j \in \mathbb{N} = \{1, 2, 3, \ldots\}$, the jth application of the KFC control strategy to the motor-pendulum system ends at time $t_{\text{e}}^{(j)} \triangleq t_{\text{f,c}}^{(j)}$. The initialisation phase ends at time $t_{\text{e}}^{(0)} \triangleq t_{\text{f,g}}^{(0)}$.

DOI: 10.1002/cta

texts, this second integration with its highly influential initial condition[§§§§] [9, 29] lies at the core of the proposed memristor-based control strategy, allowing to optimise the duration of the kick phase in a subsequent $(j+1)$th application of the KFC paradigm.

Referring to the block diagram model of the catch phase, shown in Figure 10, let us gain further insights into the instrumental role of the second non-inverting integrator path in the proposed control strategy. The second integrator, with time constant K_{int2} measured in unit s^{-1}, introduces yet another differential equation in the mathematical description of the dynamic system, namely,

$$\frac{dv_{\text{int2}}}{dt} = K_{\text{int2}} \cdot v_{\text{int1}}. \tag{25}$$

Thus, over the course of the jth catch phase, when the original GAF control paradigm is active, the non-inverting integrator provides the time integration of the inverting integrator output voltage v_{int1}. This allows the determination of the optimal time instant $t_{0,\text{f}}^{(j+1)} = t_{\text{f,k}}^{(j+1)}$ at which the fly phase should commence in a next $(j+1)$th application of the KFC strategy. Let us see how.

Importantly, previous to the first run of the KFC control approach, associated to the unitary value for j, the original GAF paradigm is initially applied to the motor-pendulum system to derive a starting estimate for $t_{\text{f,k}}^{(1)}$. This starting procedure is called initialisation phase. It corresponds to the run of a preliminary isolated catch phase. As anticipated earlier, a fictitious iteration number $j = 0$ is attributed to it. At the beginning of such phase, that is, at time $t = t_{\text{i}}^{(0)} \triangleq t_{0,\text{g}}^{(0)}$, v_{int2} is set to 0 V. Denoting the final time of the initialisation phase as $t = t_{\text{f,g}}^{(0)}$, solving Eqn 25 analytically, the expression for the non-inverting integrator output voltage at the end of the preliminary phase may be cast as

$$v_{\text{int2}}(t_{\text{f,g}}^{(0)}) = v_{\text{int2}}(t_{0,\text{g}}^{(0)}) + K_{\text{int2}} \int_{t_{0,\text{g}}^{(0)}}^{t_{\text{f,g}}^{(0)}} v_{\text{int1}}(t')dt', \tag{26}$$

where $v_{\text{int2}}(t_{\text{i}}^{(0)}) = v_{\text{int2}}(t_{0,\text{g}}^{(0)}) = 0\,\text{V}$. Now, with $t_{\text{i}}^{(1)} \triangleq t_{0,\text{k}}^{(1)}$ denoting the initial time of the first application of a KFC kick phase, the estimate number 1 for the optimal time instant $t_{\text{f,k}}^{(1)}$ is determined by imposing the following equality:

$$K_{\text{ctrl}} \int_{t_{0,\text{k}}^{(1)}}^{t_{\text{f,k}}^{(1)}} v_{\text{ctrl}}(t')dt' = v_{\text{int2}}(t_{\text{f,g}}^{(0)}), \tag{27}$$

where K_{ctrl} is yet another positive time integration constant with unit s^{-1}. Eqn 27 basically equates a scaled version of the area under the time waveform of the control voltage applied to the armature node in the first kick phase to Eqn 26, representing the first estimate for the 'work' necessary to raise the pendulum from the stable rest state to the target location. With $t_{\text{i}}^{(1)} \triangleq t_{0,\text{k}}^{(1)} = 0\,\text{s}$, recalling that $v_{\text{ctrl}}(t) = v_{\text{ctrl,max}}$ during a kick phase, the following estimate for the time instant $t_{0,\text{f}}^{(1)} = t_{\text{f,k}}^{(1)}$, at which the first fly phase should commence, may easily be determined from Eqn 27 (see also the diagram of Figure 9(a)):

$$t_{\text{f,k}}^{(1)} = \frac{1}{K_{\text{ctrl}} \cdot v_{\text{ctrl,max}}} \cdot v_{\text{int2}}(t_{\text{f,g}}^{(0)}). \tag{28}$$

[§§§§] It is important to point out that the jth run of the proposed control procedure starts always from a kick phase; thus, $t_{\text{i}}^{(j)} \triangleq t_{0,\text{k}}^{(j)}$, which, as mentioned earlier, is reset to 0 s for each $j \in \mathbb{N} = \{1, 2, 3, \ldots\}$. The initial conditions for angular velocity ω, armature current i_{A} and first inverting integrator output voltage v_{int1} are all set to the null value. Unlike the standard GAF paradigm, here, the initial value for the pendulum angle γ could be chosen as π also in the numerical simulations, because the 'kick' would push the pendulum away from its stable rest state anyways. However, for comparison purposes, $\gamma(t_{\text{i}}^{(j)})$ shall be set as in the old strategy. With regard to the second non-inverting integrator output voltage v_{int2}, it needs to be initialised to its last value at the end of the catch phase in the previous application of the strategy for each $j \in \mathbb{N} : j \neq 1$ or to its last value at the end of the run of the old GAF strategy (initialisation phase) for $j = 1$. Regarding the initialisation phase, consisting of a preliminary GAF control run (here, j is 0), it starts at time $t_{\text{i}}^{(0)} \triangleq t_{0,\text{g}}^{(0)}$, also set to 0 s. The initial conditions for ω, i_{A}, γ and v_{int1} are set to the same values as in a standard GAF control application, but here also $v_{\text{int2}}(t_{\text{i}}^{(0)})$ needs to be specified and is taken equal to 0 V.

DOI: 10.1002/cta

Typically the estimate for the time duration of a kick phase depends on the dynamic system initial conditions and on the rod topology, especially its length and load mass. For constant initial conditions and fixed values of l and m, the estimate for the time interval of the kick phase number 1 will not undergo noticeable modifications in subsequent applications of the KFC paradigm. In fact, under these ideal circumstances, for any $j \in \mathbb{N} : j > 1$, the 'kick' would be so good that the pendulum would basically attain the upright position already at the end of the kick phase, implying that the fly phase would have a time duration of null measure, and that, over the course of a catch phase, v_{int1} would not depart much from its initial null value, and, concurrently, v_{int2} would not be subject to a sensible variation as compared with its value at the end of the preceding $(j-1)$th catch phase. On the other hand, should the limb topology undergo modifications or the system initial conditions experience significant disturbances at some stage, then the last estimate of the kick phase duration would not be appropriate anymore in a later application of the strategy. However, under these circumstances, a few runs of the KFC strategy shall lead to a progressive improvement of the incorrect kick phase duration estimate, demonstrating the capability of the proposed approach to adapt to environmental changes. Let us explain this in some detail. The second integrator output voltage at the end of a jth catch phase ($j \in \mathbb{N} : j > 1$) is expressed by

$$v_{\text{int2}}(t_{\text{f,c}}^{(j)}) = v_{\text{int2}}(t_{0,\text{c}}^{(j)}) + K_{\text{int2}} \int_{t_{0,\text{c}}^{(j)}}^{t_{\text{f,c}}^{(j)}} v_{\text{int1}}(t')dt', \tag{29}$$

where the initial condition, assuming a crucial role in our control strategy and calling for the use of a memristor (see in the succeeding texts), is given by

$$v_{\text{int2}}(t_{0,\text{c}}^{(j)}) = v_{\text{int2}}(t_{0,\text{g}}^{(0)}) + K_{\text{int2}} \int_{t_{0,\text{g}}^{(0)}}^{t_{0,\text{c}}^{(j)}} v_{\text{int1}}(t')dt', \tag{30}$$

where $v_{\text{int2}}(t_{0,\text{g}}^{(0)}) = 0\,\text{V}$. Assuming that, prior to this jth application of the strategy, either the initial conditions or the rod topology were subject to variations, the jth 'kick' would then be imperfect. The first integrator output voltage would experience a non-negligible variation as it evolves from its initial null value to its final null value during the jth catch phase – the area under its time waveform over such phase would be more and more positive (negative) the weaker (stronger) the 'kick' were – leading to a concurrent significant change – specifically a more consistent increase (decrease) – in the second integrator output voltage the weaker (stronger) the 'kick' were, according to Eqn 29. However, this would lead to a proper correction of the estimate of the duration of a later $(j+1)$th kick phase, which, as shown in the succeeding texts, would be longer (shorter) the weaker (stronger) the jth 'kick' were. With $t_{\text{i}}^{(j+1)} \triangleq t_{0,\text{k}}^{(j+1)}$ denoting the initial time of the $(j+1)$th application of a KFC kick phase, equating the area under the curve of the control voltage applied at the armature node in the $(j+1)$th kick phase to the updated jth estimate for the 'work' necessary to raise the pendulum from the stable rest state to the target location (Eqn 29), that is,

$$K_{\text{ctrl}} \int_{t_{0,\text{k}}^{(j+1)}}^{t_{\text{f,k}}^{(j+1)}} v_{\text{ctrl}}(t')dt' = v_{\text{int2}}(t_{\text{f,c}}^{(j)}), \tag{31}$$

recalling that $v_{\text{ctrl}}(t) = v_{\text{ctrl,max}}$ during a kick phase and resetting to 0 s the initial time $t_{\text{i}}^{(j+1)} \triangleq t_{0,\text{k}}^{(j+1)}$, the corrected estimate for the $(j+1)$th kick phase duration is found to be given by (refer to Figure 9(a))

$$t_{\text{f,k}}^{(j+1)} = \frac{1}{K_{\text{ctrl}} \cdot v_{\text{ctrl,max}}} \cdot v_{\text{int2}}(t_{\text{f,c}}^{(j)}). \tag{32}$$

As anticipated earlier, the weaker (stronger) the jth 'kick' were, and the larger (smaller) the estimate for $t_{\text{f,k}}^{(j+1)}$ would be, confirming the adaptability of the proposed strategy to changes in the system external conditions. Similarly as for the storage of the initial condition in Eqn 30, the use of a memristor device is necessary for the achievement of this adaptability property.

Let us finalise this part I paper stressing up the fundamental role of a memristor in our approach. Importantly, during the kick and fly phases of a generic $(j+1)$th KFC control strategy application, when the non-inverting integrator gets inactive (a similar reasoning applies of course when the robot

DOI: 10.1002/cta

goes in sleep mode), the value of the voltage $v_{\mathrm{int}2}(t_{\mathrm{f,c}}^{(j)})$ at the end of the catch phase of the previous jth application of the control scheme needs to be stored in some nonvolatile memory cell, in order to allow its retrieval and use as new initial condition $v_{\mathrm{int}2}(t_{0,\mathrm{c}}^{(j+1)})$ in the non-inverting integration of $v_{\mathrm{int}1}$ during the $(j+1)$th catch phase. This calculation, also enabled by the same nonvolatile memory cell operating in computing mode, would then be used to derive an estimate for the $(j+2)$th kick phase duration[¶¶¶¶] $t_{\mathrm{f,k}}^{(j+2)}$ in terms of the second non-inverting integrator output voltage $v_{\mathrm{int}2}(t_{\mathrm{f,c}}^{(j+1)})$ at the end of the $(j+1)$th catch phase.

An ideal memristor with its nonvolatile memory capability naturally lends itself to perform history-dependent time integration. Recall in fact that, for an ideal charge-controlled memristor [7], the state variable is defined as the charge q_m flowing through it, which represents the time integral of the device current i_m over the whole past, crucially depending upon the initial condition $q_m(t_{\mathrm{i}})$ at a given starting time $t = t_{\mathrm{i}}$, according to

$$q_{\mathrm{m}}(t) = q_m(t_{\mathrm{i}}) + \int_{t_{\mathrm{i}}}^{t} i_{\mathrm{m}}(t')dt' \tag{33}$$

A charge-controlled memristor of this kind is ideally suitable for the circuit implementation of the non-inverting integrator-based branch of the block diagram model of Figure 10. In fact, Eqn 33 may be used to integrate the inverting integrator output voltage $v_{\mathrm{int}1}$ provided a current proportional to it (with proportionality factor measured in unit s) is let flowing through the nonvolatile memory cell. The details are discussed in the companion part II paper[‖‖‖‖‖‖] [40].

4. CONCLUSIONS AND FUTURE RESEARCH DEVELOPMENTS

The Myon [37] is a humanoid robot in which each joint is controlled independently by a CSL, a built-in CMOS-based bio-inspired ANN, which is trained through an attractor-based behaviour control learning scheme [38] to correct a number of distinct actions according to external stimuli. One of the control strategies implementable by this supervised loop allows the movement of the limb connected to a joint from a stable rest state up to a certain height and the maintenance of this new position afterwards till a particular time of interest. The original approach adopted for this control process, known as Go-Against-the-Force (GAF) paradigm, is robust and stable but results in slow and energy-inefficient limb movements. The complex nonlinear dynamics [50, 51] and learning capability [28] of memristors [52] as well as their fascinating ability to process information and store data in the same physical location may be exploited to devise innovative circuits complementing and/or extending the functionalities of conventional CMOS electronic systems. This two-part manuscript proposes a novel, low-power, time-efficient and adaptive memristor-centre strategy for the aforementioned robot action correction, named KFC paradigm. In this part I paper, we introduced the theoretical foundations of the novel control approach pointing out its advantages over the original strategy. In the part II paper [40], a hybrid CMOS/memristor closed-loop circuit implementation for the new control paradigm is developed, first using an ideal memristor emulator [41] and then a real memristor nanodevice from Knowm, Inc. [43]. The study presented in [40], based upon numerical simulations of mathematical models, reveals the benefits of the memristor-based feedback circuit over the original purely CMOS control electronic system in terms of energy, and speed, as well as its inheritance from the standard counterpart of a good level of adaptability to modifications in the limb load. The theoretic and numerical investigations in this two-part paper justify our long-term commitment to devote further research efforts to the imple-

[¶¶¶¶] In the actual circuit implementation of the KFC strategy, the estimate for the time duration of a kick phase shall be carried out online during the kick phase itself (see the companion paper [40] for details).

[‖‖‖‖‖‖] Despite the significant progress in memristor technology over the past few years, a device capable to perform an accurate time integration is not yet available. For this reason, in the circuit implementation of the KFC paradigm based upon the model of a real nanodevice, we shall adopt a different methodology to derive an estimate for the time duration of a kick phase. On the other hand, the non-inverting integration-based approach, illustrated in the block diagram model of Figure 10, shall be followed in the circuit realisation of the KFC paradigm based upon an ideal memristor emulator. All details are reported in the part II manuscript [40].

DOI: 10.1002/cta

mentation of the KFC control strategy in a practical memristor circuit. All in all, together with other major works on sensing [53, 54] as well as on memcomputing [55] and logics [56, 57], this study provides a clear example of the multifaceted opportunities for scientific progress offered by memristors, besides the mainstream applications regarding nonvolatile memory design and neuromorphic system development.

ACKNOWLEDGEMENTS

The support from EU COST Action IC1401 is acknowledged. We also thank the Deutsche Forschung Gesellschaft (DFG) for their financial contribution to the research project 'Locally active memristive data processing (LAMP)' under grant number TE 257/22-1. L. O. Chua's research is supported by AFOSR grant FA 9550-13-1-0136.

REFERENCES

1. Chua LO, Desoer CA, Kuh EA. *Linear and Nonlinear circuits*. McGraw Hill: New York, 1985.
2. Chua LO. Memristor – the missing circuit element. *IEEE Trans. on Circuit Theory* 1971; **18**(5):507–519.
3. Corinto F, Chua LO, Civalleri PP. A theoretical approach to memristor devices. *IEEE Journal on Emerging and Selected Topics in Circuits and Systems* 2015; **5**(2):123 – 132.
4. Strukov DB, Snider GS, Stewart DR, Williams RS. The missing memristor found. *Nature* 2008; **453**:80–83.
5. Biolek D, Biolek Z, Biolkova V. Pinched hysteretic loops of ideal memristors, memcapacitors and meminductors must be self-crossing. *Electronics Letters* 2011; **47**(25):1385–1387.
6. Ascoli A, Schmidt T, Tetzlaff R, Corinto F. Application of the Volterra series paradigm to memristive systems. In *Memristors and Memristive Systems*, Tetzlaff R (ed.), chapter 5. Springer: New York, 2014; 163–191.
7. Chua LO. Everything you wish to know about memristors but are afraid to ask. *RadioEngineering* 2015; **24**(2): 319–368.
8. Corinto F, Forti M. Memristor circuits: flux–charge analysis method. *IEEE Trans. on Circuits and Systems – I: Regular Papers* 2016; **63**(11):1997–2009.
9. Corinto F, Forti M. Memristor circuits: bifurcations without parameters. *IEEE Trans. on Circuits and Systems – I: Regular Papers* 2017; **64**(6):1540–1551.
10. Di Marco M, Forti M, Innocenti G, Tesi A. Harmonic balance method to analyze bifurcations in memristor oscillatory circuits. *Int. J. Circuit Theory and Applications* 2017. https://doi.org/10.1002/cta.2414.
11. Chua LO. If it's pinched, it's a memristor. *Special issue on memristive devices, semiconductor science and technology* 2014; **29**(10):104001.
12. Picos R, Stavrinides SG, Theodorakakos A. The experimental model of a non-ideal memristor. *IEEE International Conference on Modern Circuits and Systems Technologies (MOCAST)* 2016. https://doi.org/10.1109/MOCAST.2016.7495165.
13. Itoh M, Chua LO. Memristor oscillators. *International Journal of Bifurcation and Chaos* 2008; **18**(11):3183–3206.
14. Zidan MA, Omran H, Smith C, Syed A, Radwan A, Gomaa A, Salama KN. A family of memristor-based reactanceless oscillators. *International Journal of Circuit Theory and Applications* 2014; **42**(11):1103–1122.
15. Corinto F, Ascoli A, Gilli M. Nonlinear dynamics of memristor oscillators. *IEEE Trans. Circuits and Systems – I* 2011; **58**(6):1323–1336.
16. Ascoli A, Tetzlaff R, Biey M, Chua LO. Complex dynamics in circuits with memristors. *Proc. Eur. Conference of Circuit Theory and Design (ECCTD)*, Vol. 4, Catania, Italy, 2017.
17. Ascoli A, Corinto F, Tetzlaff R. Generalized boundary condition memristor model. *International Journal of Circuit Theory and Applications* 2016; **44**(1):60–84.
18. Jo SH, Chang T, Ebong I, Bhadviya BB, Mazumder P, Lu W. Nanoscale memristor device as synapse in neuromorphic systems. *Nano Letters* 2010; **10**(4):1297–1301.
19. Thomas A. Memristor-based neural networks. *Journal of Physics D: Applied Physics* 2013; **46**(9):093001.
20. Corinto F, Ascoli A, Young-Su K, Kyeong-Sik M. Cellular nonlinear networks with memristor synapses. In *Memristor Networks*, Adamatzky A, Chua LO (eds), chapter 13. Springer International Publishing: AG, Cham, Switzerland, 2014; 267–291.
21. Guo X, Merrikh-Bayat F, Gao L, Alibart F, Hoskins B, Theogarajan L, Teuscher C, Linares-Barranco B, Strukov D. Modeling and experimental demonstration of a Hopfield network analog-to-digital converter with hybrid CMOS/memristor circuits. *Frontiers in Neuroscience* 2015; **9**(488):1–8.
22. Pershin YV, Di Ventra M. Practical approach to programmable analog circuits with memristors. *IEEE Trans. on Circuits and Systems – I: Regular Papers* 2010; **57**(8):1857–1864.
23. Ascoli A, Tetzlaff R, Corinto F, Mirchev M, Gilli M, Memristor-based filtering applications. *14th Latin American Test Workshop (LATW)*, Cordoba, Argentina, 2013; 1–6.
24. Driscoll T, Quinn J, Klein S, Kim HT, Kim BJ, Pershin YV, Di Ventra M, Basov DN. Memristive adaptive filters. *Applied Physics Letters* 2010; **97**(9):093502.
25. Wang X, Zhao Y, Liao Y. Dynamic performance analysis of PID controller with one memristor. *International Conference on Information Science and Technology*, Nanjing, China, 2011; 1234–1237.

26. Dòria-Cerezo A, van der Heijden L, Scherpen JMA. Memristive port-Hamiltonian control: path-dependent damping injection in control of mechanical systems. *European Journal of Control* 2013; **19**(6):454–460.
27. Ascoli A, Tetzlaff R, Chua LO, Strachan JP, Williams RS. History erase effect in a non-volatile memristor. *IEEE Trans. Circuits and Systems-I: Reg. Papers* 2016; **63**(3):389–400.
28. Tzouvadaki I, Jolly P, Lu X, Ingebrandt S, de Micheli G, Estrela P, Carrara S. Label-free ultrasensitive memristive aptasensor. *Nanoletters* 2016; **16**(7):4472–4476.
29. Corinto F, Ascoli A, Gilli M. Analysis of current–voltage characteristics for memristive elements in pattern recognition systems. *Int. J. Circuit Theory Appl.* 2012; **40**(12):1277–1320.
30. Ascoli A, Slesazeck S, Mähne H, Tetzlaff R, Mikolajick T. Nonlinear dynamics of a locally-active memristor. *IEEE Trans. Circuits Syst. I: Reg. Papers* 2015; **62**(4):1165–1175.
31. Talati N, Gupta S, Mane P, Kvatinsky S. Logic design within memristive memories using memristor aided loGIC (MAGIC). *IEEE Transactions on Nanotechnology* 2016; **15**(4):635–650.
32. Brooks RA. Prospects for human level intelligence for humanoid robots. *Proceedings of the First International Symposium on Humanoid Robots (HURO-96)*, Tokyo (Japan), 1996.
33. Koenig N, Matarić MJ. Robot life-long task learning from human demonstrations: a Bayesian approach. *Autonomous Robots* 2016:1–16.
34. Hild M. Defying gravity – a minimal cognitive sensorimotor loop which makes robots with arbitrary morphologies stand up. *11th International Conference on Accomplishments in Electrical and Mechanical Engineering and Information Technology (DEMI)*, Banja Luka, Bosnia and Herzegovina, 2013; 23–34.
35. Kim JY, Park IW, Ho JH. Walking control algorithm of biped humanoid robot on uneven and inclined floor. *Journal of Intelligent and Robotic Systems* 2007; **48**(4):457–484.
36. Koolen T, Bertrand S, Thomas G, de Boer T, Wu T, Smith J, Englsberger J, Pratt J. Design of a momentum-based control framework and application to the humanoid robot Atlas. *International Journal of Humanoid Robotics* 2016; **13**(1):1650007.
37. Hild M, Siedel T, Benckendorff C, Kubisch M, Thiele C. Myon: concepts and design of a modular humanoid robot which can be reassembled during runtime. *Proceedings of the 14th International Conference on Climbing and Walking Robots and the Support Technologies for Mobile Machines*, Paris, France, 2011; 45–52.
38. Hild M, Kubisch M. Self-exploration of autonomous robots using attractor-based behavior control and ABC-learning. *11th Scandinavian Conference on Artificial Intelligence (SCAI)*, Trondheim, Norway, 2011.
39. Hild M. Roboter mit robustem Verhalten. *Bulletin* 2013; **10s**:12–15.
40. Baumann D, Ascoli A, Tetzlaff R, Chua LO, Hild M. Memristor-enhanced humanoid robot control system – part II: circuit theoretic model and performance analysis. *Int. Journal of Circuit Theory and Applications (IJCTA)* 2017. https://doi.org/10.1002/cta.2430.
41. Kim H, Sah MPd, Yang C, Cho S, Chua LO. Memristor emulator for memristor circuit applications. *IEEE Transactions on Circuits and Systems – I: Regular Papers* 2012; **59**(10):2422–2431. https://doi.org/10.1002/cta.2430.
42. Molter TW, Nugent A. The generalized metastable switch memristor model. *15th International Workshop on Cellular Nanoscale Networks and their Applications (CNNA)*, Dresden, Germany, VDE Verlag, 2016.
43. Available from: http://knowm.org, 2017.
44. Ascoli A, Tetzlaff R, Chua LO, Yi W, Williams RS. Memristor emulators: a note on modeling. In *Advances in Memristors, Memristive Devices and Systems*, vol. 701, Vaidyanathan S, Volos C (eds), Studies in Computational Intelligence. Springer International Publishing AG: Cham, Switzerland, 2017; 1–17.
45. Linear Technology. *LTspice IV getting started guide*, 2011. Available from: http://cds.linear.com/docs/en/software-and-simulation/LTspiceGettingStartedGuide.pdf, 2017.
46. Yildiz AB. Electrical equivalent circuit based modeling and analysis of direct current motors. *Int. J. of Electrical Power & Energy Systems* 2012; **43**(1):1043–1047.
47. Schröder D. *Elektrische Antriebe–Grundlagen, 5., erweiterte Auflage*. Springer Vieweg: Wiesbaden, Germany, 2013. ISBN: 978-3-642-30470-5.
48. Available from: https://www.faulhaber.com/de/produkte/serie/2619sr/, 2017.
49. Pontryagin LS. *The Mathematical Theory of Optimal Processes*, Classics of Soviet Mathematics. Gordon and Breach Science Publishers: S.A., Montreux; Switzerland, 1986. ISBN-13: 978-2881240775.
50. Ascoli A, Tetzlaff R, Chua LO. The first ever real bistable memristors – part I: theoretical insights on local fading memory. *IEEE Transactions on Circuits and Systems-II: Express Briefs* 2016; **63**(12):1091–1095.
51. Ascoli A, Tetzlaff R, Chua LO. The first ever real bistable memristors – part II: design & analysis of a local fading memory system. *IEEE Transactions on Circuits and Systems-II: Express Briefs* 2016; **62**(12):1096–1100.
52. Chua LO. Resistance switching memories are memristors. *Applied Physics A* 2011; **102**:765–783.
53. Tzouvadaki I, Aliakbarinodehi N, De Micheli G, Carrara S. Memristive effect as a novelty in drug monitoring. *Nanoscale* 2017; **9**(27):9676–9684. https://doi.org/10.1039/C7NR01297G.
54. Ibarlucea B, Akbar TF, Kim K, Rim T, Baek CK, Ascoli A, Tetzlaff R, Baraban L, Cuniberti G. Ultrasensitive detection of Ebola matrix protein in a memristor mode. *NanoResearch,* Tsinghua University Press 2017. https://doi.org/10.1007/s12274-017-1720-2.
55. Ascoli A, Tetzlaff R, Ielmini D, Chua LO. Cellular Nonlinear Networks with real-world memristors: a paradigm for mem-computing, 5th Workshop on Memristor Technology, Design, Automation and Computing (mDAC). *HiPEAC Conference, invited talk*, Manchester, 24 Jan. 2018.
56. Kvatinsky S, Belousov D, Liman S, Satat G, Wald N, Friedman EG, Kolodny A, Weiser UC. MAGIC – memristor aided LoGIC. *IEEE Transactions on Circuits and Systems II: Express Briefs* 2014; **61**(11):1–5.

57. Ben Hur R, Wald N, Talati N, Kvatinsky S. SIMPLE MAGIC: synthesis and in-memory MaPping of logic execution for memristor-aided loGIC. *IEEE/ACM Int. Conf. on Computer-Aided Design (ICCAD)*, Irvine, California, USA, 2017.
58. Reshmin SA. Bifurcation in a time-optimal problem for a second-order non-linear system. *Journal of Applied Mathematics and Mechanics* 2009; **73**(4):403–410.
59. Reshmin SA, Chernousko FL. Properties of the time-optimal feedback control for a pendulum-like system. *Journal of Optimization Theory and Applications* 2014; **163**(1):230–252.
60. Bellman R, Glicksberg I, Gross O. On the bang-bang control problem. *Quarterly of Applied Mathematics* 1956; **14**(1):11–18.

APPENDIX A: IMPLEMENTATION OF THE GO-AGAINST-THE-FORCE PARADIGM ON HARDWARE

A motor-pendulum system under Go-Against-the-Force (GAF) control was fabricated in house. The schematics of the hardware realisation of the GAF control loop of Figure 2(a) is shown in Figure A.1. The hardware GAF cognitive sensorimotor loop system consists of four stages (enclosed within rectangular boxes in red dashed line style) and a switch, referred to as S_{gaf}, and crucially interacts with a motor with combined sensor–actuator role. The armature voltage is calculated as $v_{\text{A}} = v_{\text{motor1}} - v_{\text{motor2}}$, where, unlike the circuit model (refer to Figure 5(b)), as shown shortly, v_{motor2} is not the ground voltage here. The leftmost stage is the cascade between a voltage divider and a voltage follower consisting of op amp $K_{1\text{A}}$. The output voltage of this stage is half the maximum operating voltage v_{B+}, set here to the supply level of 9 V. The voltage follower output signal is applied to the positive input of the op amp $K_{1\text{B}}$ in the second inverting integrator stage, including also a resistor–capacitor parallel one port in the op amp feedback loop, and to the positive input of the op amp $K_{2\text{B}}$ in the rightmost stage, which, together with the third stage with op amp $K_{2\text{A}}$, implements the impedance conversion. Thus, unlike in the LTSpice simulations of the circuit-theoretic model of Figure 5(c), here, initially, the integrator output voltage v_{int1} (as well as v_{motor1} and v_{motor2}) is not null but sits half way between ground and supply, that is, its level is set to $v_{B+}/2 = 4.5\,\text{V}$ at start. In the sense phase, when the switch S_{gaf} in Figure A.1 is set to the opposite configuration, if the voltage v_1, sampled from the left terminal of the motor and appearing at the right terminal of resistor R_5, gets larger than $v_{B+}/2$, the inverting integrator output voltage shall decrease; otherwise, it will increase (in any case v_{int1} lies in $[0\,\text{V}, v_{B+}]$ at all times, that is, unlike in the LTSpice simulations of the circuit-theoretic model of the overall dynamic system, it never goes negative here). To enable the motor motion in both directions, the voltage at its right terminal is fixed to $v_{B+}/2$ through the use of the last stage. In the drive phase, when the switch S_{gaf} assumes the

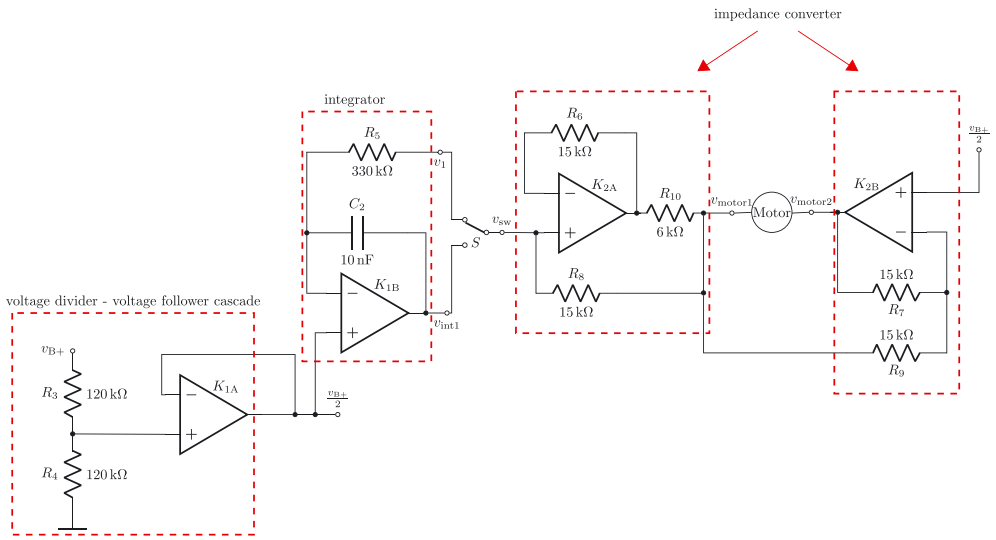

Figure A.1. Schematics of the hardware implementation of the Go-Against-the-Force control system of Figure 2(a). [Colour figure can be viewed at wileyonlinelibrary.com]

DOI: 10.1002/cta

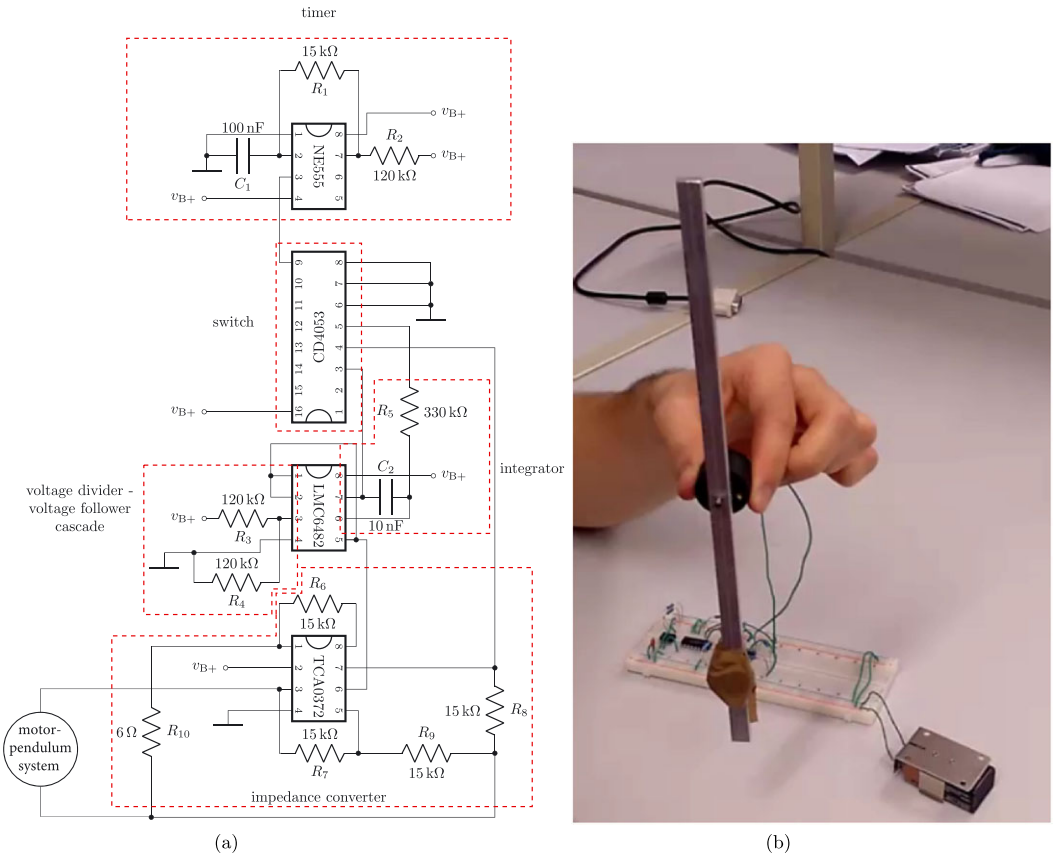

Figure A.2. (a) Integrated circuit-based set-up of the cognitive sensorimotor loop circuitry implementing the Go-Against-the-Force strategy to control the motor-pendulum system (the loaded rod attached to the motor is not shown here). The op amps' supply levels are 0 and 9 V. (b) Hardware prototype of the inverted pendulum under Go-Against-the-Force cognitive sensorimotor loop circuitry control. [Colour figure can be viewed at wileyonlinelibrary.com]

configuration shown in Figure A.1, the third stage transfers the DC voltage appearing at the inverting integrator output at the end of the sense phase to the left terminal of the motor. If v_{motor1} is below $v_{B+}/2$, the armature voltage dropping across the two motor terminals gets negative; otherwise, it goes positive. As a result, the pendulum may move both in the clockwise and in the counterclockwise direction. The switch S_{gaf}, responsible for the transitions between sense and drive phases, is controlled by a pulse-based voltage signal generated by the timer IC NE555, which is omitted from Figure A.1, whereas is visible in plot (a) of Figure A.2, showing the integrated circuit-based set-up of the GAF cognitive sensorimotor loop electronic system controlling the motor-pendulum system. The supply levels of the op amps within the integrated circuits are***** 0 and 9 V. Figure A.2(b) depicts the final working hardware prototype of the controlled system, including a loaded rod attached to the motor.

APPENDIX B: APPLICATION OF THE MAXIMUM PRINCIPLE OF PONTRYAGIN

The objective of this section is to choose an optimal positive-valued time waveform for the control voltage $v_{\text{ctrl}}(t)$ to apply†††††† to the armature node A so as to induce a time-efficient and energy-efficient

*****In the parameter/input/initial condition set-up, extra care was taken to ensure that no signal within the circuit theoretic model of the motor-pendulum system under GAF control, that is, within the ensemble of circuits in Figures 4(b) and (c) and 5, ever exceeded the [0, 9]V range in all LTSpice simulations.

††††††It is noteworthy to observe that the armature node is driven by a certain control voltage v_{ctrl} during a control phase, while assumes the same voltage v_{ind} appearing between the motor terminals under no control.

DOI: 10.1002/cta

movement of a robot's limb from the stable rest state $\gamma = 0$ to the upright position $\gamma = \pi$ over the time interval $[t_\mathrm{i},\ t_\mathrm{e}]$. Ideally, no further control action would be required after the time instant t_e, because, due to static friction, the limb would maintain the upright position after attaining it. In order to achieve the aforementioned objective, we apply the maximum principle of Pontryagin [49] to the dynamic system expressed by Eqns 9–11. Let $v_\mathrm{ctrl}(t)$ assume positive values in $\left[v_\mathrm{ctrl,min}, v_\mathrm{ctrl,max}\right]$ over $[t_\mathrm{i},\ t_\mathrm{e}]$. Here, we derive an optimal time waveform for the control voltage by minimising the following cost function

$$\mathcal{J} = \int_{t_\mathrm{i}}^{t_\mathrm{e}} f_0\left(v_\mathrm{ctrl}(t)\right) dt, \tag{B.1}$$

where $f_0(\cdot)$ denotes a function to be defined according to the type of optimisation of choice (see later for details).

In our problem, the state vector $\vec{x}(t)$ is expressed by

$$\vec{x}(t) = \begin{pmatrix} \gamma(t) \\ \omega(t) \\ i_\mathrm{A}(t) \end{pmatrix}. \tag{B.2}$$

At the beginning, that is, at $t = t_\mathrm{i}$, the pendulum is in the stable equilibrium; therefore,

$$\vec{x}(t_i) = \vec{x}_\mathrm{i} = \begin{pmatrix} \pi \\ 0 \\ 0 \end{pmatrix}. \tag{B.3}$$

The goal position at $t = t_\mathrm{e}$ may be expressed with the vector

$$\vec{x}\left(t_\mathrm{e}\right) = \vec{x}_\mathrm{e} = \begin{pmatrix} 0 \\ 0 \\ 0 \end{pmatrix}. \tag{B.4}$$

A Hamiltonian function is now defined over $t \in \left[t_\mathrm{i}, t_\mathrm{e}\right]$ with the following form:

$$H\left(\vec{x}(t), v_\mathrm{ctrl}(t), \vec{\psi}(t), \lambda_0\right) = \lambda_0 f_0\left(v_\mathrm{ctrl}(t)\right) + \left(\vec{\psi}(t)\right)^T \vec{f}\left(\vec{x}(t), v_\mathrm{ctrl}(t)\right), \tag{B.5}$$

where the constant λ_0 assumes values in $\{0, 1\}$, $\vec{\psi}(t) = \left(\psi_1(t), \psi_2(t), \psi_3(t)\right)^T$ represents a piecewise continuously differentiable function, and $\vec{f}(\cdot,\cdot)$ denotes the time derivative of the state vector, that is,

$$\dot{\vec{x}}(t) = \vec{f}\left(\vec{x}(t), v_\mathrm{ctrl}(t)\right), \tag{B.6}$$

expressed in our case by Eqns 9–11 with $v_\mathrm{A}(t) = v_\mathrm{ctrl}(t)$. The maximum principle of Pontryagin states that, under an optimal choice for the control signal[‡‡‡‡‡] – let us call it $v^*_\mathrm{ctrl}(t) - \forall t \in \left[t_\mathrm{i}, t_\mathrm{e}\right]$, there exists a vector

$$\begin{pmatrix} \lambda^*_0 \\ \vec{\psi}^*(t) \end{pmatrix} \neq \vec{0}, \tag{B.7}$$

such that the following conditions are fulfilled:

$$\dot{\vec{x}}^*(t) = \vec{f}\left(\vec{x}^*(t), v^*_\mathrm{ctrl}(t)\right) \quad \forall\, t \in \left[t_i, t_\mathrm{e}\right], \tag{B.8a}$$

$$\vec{x}^*(t_i) = \vec{x}_\mathrm{i}, \tag{B.8b}$$

[‡‡‡‡‡]Throughout this appendix, an optimal choice for a variable is indicated by endowing its symbol with an asterisk subscript.

DOI: 10.1002/cta

$$\vec{x}^*(t_e) = \vec{x}_e, \tag{B.8c}$$

$$\dot{\vec{\psi}}^*(t) = -\left(\frac{\partial \vec{f}\left(\vec{x}^*(t), v^*_{ctrl}(t)\right)}{\partial \vec{x}}\right)^T \vec{\psi}^*(t) \quad \forall\, t \in \left[t_i, t_e\right], \tag{B.8d}$$

$$H\left(\vec{x}^*(t), v^*_{ctrl}(t), \vec{\psi}^*(t), \lambda^*_0\right) \leq H\left(\vec{x}^*(t), v_{ctrl}(t), \vec{\psi}^*(t), \lambda^*_0\right) \quad \forall\, v_{ctrl} \in \left[v_{ctrl,min}, v_{ctrl,max}\right] \quad \forall\, t \in \left[t_i, t_e\right], \tag{B.8e}$$

$$H\left(\vec{x}^*\left(t_e\right), v^*_{ctrl}\left(t_e\right), \vec{\psi}^*\left(t_e\right), \lambda^*_0\right) = 0. \tag{B.8f}$$

Before proceeding, we need to define a closed form for the function $f_0(\cdot)$. Choosing the time duration of the control system operation as the target of our optimisation procedure, it is reasonable to express $f_0(\cdot)$ simply as

$$f_0\left(v_{ctrl}(t)\right) \triangleq 1. \tag{B.9}$$

This selection implies that the cost function $\mathcal{J}$ in Eqn B.1 reduces to the time interval $\Delta t_{ctrl} = t_e - t_i$ of the control phase. Inserting the definition of the Hamiltonian, reported in Eqn B.5, into inequality B.8e, inserting Eqn B.9 in place for $f_0(\cdot)$ and using the state Eqns 9–11, $\forall\, v_{ctrl} \in \left[v_{ctrl,min}, v_{ctrl,max}\right]$ and $\forall\, t \in \left[t_i, t_e\right]$, we obtain:

$$\begin{aligned}
&\psi^*_2(t)\frac{c\cdot\varphi\cdot i^*_A(t) - m\cdot g\cdot l\cdot\sin(\gamma^*(t)) - B_m\omega^*(t)}{J} + \psi^*_3(t)\frac{v^*_{ctrl}(t) - R_A i^*_A(t) - c\cdot\varphi\cdot\omega^*(t)}{L_A} - \psi^*_1(t)\omega^*(t)\\
&\leq \psi^*_2(t)\frac{c\cdot\varphi\cdot i^*_A(t) - m\cdot g\cdot l\cdot\sin(\gamma^*(t)) - B_m\omega^*(t)}{J} + \psi^*_3(t)\frac{v_{ctrl}(t) - R_A i^*_A(t) - c\cdot\varphi\cdot\omega^*(t)}{L_A} - \psi^*_1(t)\omega^*(t),
\end{aligned} \tag{B.10}$$

leading to

$$\psi^*_3(t)\frac{v^*_{ctrl}(t)}{L_A} \leq \psi^*_3(t)\frac{v_{ctrl}(t)}{L_A}. \tag{B.11}$$

Solving inequality B.11 for the optimal control signal yields[§§§§§]

$$v^*_{ctrl}(t) = \begin{cases} v_{ctrl,max} & \text{for } \psi^*_3(t) < 0, \\ v_{ctrl,min} & \text{for } \psi^*_3(t) \geq 0. \end{cases} \tag{B.12}$$

An optimal control [58] can thus be achieved through the use of a switch enforcing the voltage at the armature node A to transition between the maximum and minimum admissible values for the control voltage, depending upon the zero crossings of the piecewise continuously differentiable function $\psi^*_3(t)$. The numerical derivation of the vector $\vec{\psi}^*(t)$, whose time evolution is governed by Eqn B.8d, may be a prohibitive task. Luckily, it is unnecessary here. In fact it has been recently demonstrated [59] that, provided the motor torque M is larger than algebraic sum of the other two torques M_L and M_F at all times over the control phase, the cost function B.1 may be minimised by inducing a single voltage transition at the armature node A through the application of a control signal of the following form:

$$v^*_{ctrl}(t) = \begin{cases} v_{ctrl,max} & \text{for } t \in [t_i, t^*) \\ v_{ctrl,min} & \text{for } t \in [t^*, t^*_e], \end{cases} \tag{B.13}$$

[§§§§§]For $\psi^*_3(t)$ equal to 0 inequality, B.11 holds for any value of $v_{ctrl} \in \left[v_{ctrl,min}, v_{ctrl,max}\right]$. Nonetheless, in this case, the control voltage is set to its lower bound, as reported in Eqn B.12.

DOI: 10.1002/cta

where t^* is the optimal time instant at which the transition occurs. This time instant should be chosen so that in the first control phase, the angle γ would experience a significant decrease from the starting value of π but would keep larger than 0. Only in the second control phase the pendulum would approach the upright position, which in the ideal case would be maintained thereafter due to static friction. In the practical case, the inherently unstable equilibrium $\bar{\gamma} = 0$ needs to be stabilised once the pendulum attains the desired position. On the basis of these theoretical results, omitting the asterisk symbol from the superscript of the aforementioned optimal time instants for simplicity, in the jth run ($j \in \mathbb{N} \in \{1, 2, 3, \dots\}$), our new control paradigm first calls for the application of the maximum control voltage $v_{\text{ctrl,max}}$ (here set to the largest allowable DC voltage v_{B_+} in the control circuit, that is, the supply level of 9 V) to the armature node A over the time interval $t \in [t_{0,\text{k}}^{(j)}, t_{\text{f,k}}^{(j)})$ (kick phase), inducing a large decrease in the angle γ, which, however, should keep positive in principle.[¶¶¶¶¶] Then, over the time interval $t \in [t_{0,\text{f}}^{(j)}, t_{\text{f,f}}^{(j)})$ with $t_{0,\text{f}}^{(j)} \triangleq t_{\text{f,k}}^{(j)}$, no control is actually applied to the motor-pendulum system – thus v_{A} coincides with v_{ind} – and the pendulum is left free to continue its ascent towards the upright position (fly phase). At the time instant $t_{\text{f,f}}^{(j)}$, when either the pendulum axial velocity vector $\vec{v}$ changes polarity (here, the 'kick' was too weak) or increases in modulus (here, the pendulum has passed over the desired position and is about to move down again from the negative side of the x axis (Figure 8(c))), the original GAF paradigm is applied to the system to stabilise the pendulum upright position (catch phase, running over a time interval $t \in [t_{0,\text{c}}^{(j)}, t_{\text{f,c}}^{(j)}]$, where $t_{0,\text{c}}^{(j)} \triangleq t_{\text{f,f}}^{(j)}$, and $t_{\text{f,c}}^{(j)}$ denotes the last time instant where the limb should be kept in the target position). The novel strategy, which we thus name 'Kick-Fly-Catch' paradigm (see the text discussion in Section 3 as well), allows to induce faster robot limb movements under a lower energy budget as compared with the GAF strategy and further endows the control system with the capability to adapt to changes in the external environment, a feature, which, for the sake of truthfulness, is present also in the original approach (see the companion part II paper [40] for details). It is important to observe that, before the first application of the proposed strategy, a preliminary run of the old paradigm (initialisation phase) is carried out to derive an initial estimate for the work necessary to raise the pendulum from the stable state to the unstable position. This estimate is then used to select the time duration for the kick phase in the first application of the proposed KFC strategy (see Section 3 for details). As a final note, it is instructive to point out that the problem of finding a time-optimal control for a given system has been widely studied in the literature. To address this issue, 'bang-bang controllers' [60], in which the control signal switches between a minimum and a maximum value, are frequently used. It is by now clear that the proposed KFC strategy adopts a similar principle.

[¶¶¶¶¶] Note that, should the angle γ go negative during a kick phase, our control strategy would work fine as well. In fact, in a scenario of this kind, the fly phase would have a time duration of null measure, and the catch phase would bring the pendulum back to the upright position, stabilising it there afterwards.

DOI: 10.1002/cta